

REVIEWS OF TOPICAL PROBLEMS PACS numbers: 98.62.Js, 98.62.Mw

Interferometric observations of supermassive black holes in the millimeter wave band

P B Ivanov, E V Mikheeva, V N Lukash, A M Malinovsky, S V Chernov, A S Andrianov, V I Kostenko, S F Likhachev

DOI: https://doi.org/10.3367/UFNe.2018.03.038308

Contents

Abstract. **We present a theoretical description of different types of accretion disks and jets near supermassive black holes (SMBHs) that can be observed in the (sub)millimeter wave band. Special attention is paid to the possible formation of the shadow of a black hole illuminated by an accretion disk or a jet. We suggest a simple criterion for identifying such a shadow in current and planned SMBH observations using very long baseline interferometry (VLBI). As an example, we propose a number of potential SMBH candidates satisfying this criterion for observations with the future Millimetron space observatory in the VLBI regime and with the Event Horizon Telescope.**

Keywords: interferometry, millimeter and submillimeter wavelengths, black holes, supermassive black hole, accretion, accretion disk, jet

P B Ivanov [(1)], **E V Mikheeva** [(2)], **V N Lukash** [(3)], **A M Malinovsky** [(4)], **S V Chernov** [(5)], **A S Andrianov** [(6)], **V I Kostenko** [(7)], **S F Likhachev** [(8)]
Astro Space Center, Lebedev Physical Institute,
Russian Academy of Sciences,
ul. Profsoyuznaya 84/32, 117997 Moscow, Russian Federation
E-mail: [(1)] pbi20@cam.ac.uk, [(2)] helen@asc.rssi.ru, [(3)] lukash@asc.rssi.ru,
[(4)] ingirami@gmail.com, [(5)] chernov@lpi.ru,
[(6)] andrian@asc.rssi.ru, [(7)] vkostenko@asc.rssi.ru,
[(8)] slikhach@asc.rssi.ru

Received 1 February 2018
Uspekhi Fizicheskikh Nauk **189** (5) 449 – 477 (2019)
DOI: https://doi.org/10.3367/UFNr.2018.03.038308
Translated by M Zh Shmatikov; edited by A M Semikhatov

1. Introduction

A task that is currently of utmost interest for modern astrophysics is to develop and implement observational programs to explore accreting supermassive black holes (SMBHs) in the millimeter wave band using the method of very long baseline interferometry (VLBI). A specific feature of this wave band is that plasma near the event horizon can be optically thin in many sources, allowing one to hope that the image of the black hole (or its 'shadow') can be directly discovered using VLBI methods. On the other hand, the attained resolution, which is of the order of several tens of millionths of an arc second (ang. μs), is comparable to the dimensions of the shadows of black holes of the largest angular size, such as those in the centers of our Galaxy and M 87.

The most ambitious observational projects in this area are the Event Horizon Telescope (EHT) and the Millimetron, the Russian space mission that is currently under development. Millimetron's predecessor is the RadioAstron, the project currently being conducted to observe the same objects in the centimeter wave band. We briefly discuss the main specific features of both experiments and make a comparative analysis of their resolving power and sensitivity.

The EHT is an interferometric array of existing (and planned) ground-based stations that conduct observations in the millimeter and submillimeter ranges of the spectrum. This array includes the Large Millimeter Telescope (LMT) and the Atacama Large Millimeter Array (ALMA) (a complete list of the facilities under operation and construction can be found at http://www.eventhorizontelescope.org/array/index.html). Beginning in 2006, the EHT has been under continuous development, which is scheduled to continue until 2020.

Although the EHT resolving power is limited by Earth's dimensions, it is sufficient for resolving angular scales of the order of the gravitational radius of the black hole located in the center of our Galaxy (about 5 ang. μs) and the galaxy M 87 (about 3.7 ang. μs). Thus, this provides the first opportunity to directly observe images of some SMBHs closest to Earth in the form of so-called shadows. It is planned to use the facilities incorporated into the EHT project as a ground-based component of the Millimetron project.

The RadioAstron project is a ground–space observatory whose space component (the Spektr-R satellite with a radio telescope aboard that has a parabolic receiving antenna 10 meters in diameter) was launched in 2011. The satellite has a highly elliptic orbit that significantly evolves under the Moon's effect; the apogee is around 340,000 km, and the orbital period is about 8 days. The RadioAstron operates in the frequency range 0.327–25 GHz, which corresponds to the wavelengths 92–1.2 cm. A large number of Russia-based and foreign radio telescopes participate in the observations. A detailed description of the system and the current state of research conducted using the RadioAstron can be found at www.radioastron.ru (see also the project description at http://www.asc.rssi.ru/radioastron/documents/docs.html).

The Millimetron project is in some aspects similar to the RadioAstron space experiment (www.asc.rssi.ru/radioastron) and, in other aspects, to the EHT. Like the RadioAstron, when operating in the VLBI observation mode, the Millimetron is a ground–space system. In comparison with the EHT, which is an interferometric array of ground-based observatories, the Millimetron is similar to it in the frequency range it uses and its sensitivity. However, the Millimetron features a much higher resolving power than the two projects; in particular, observations will be conducted at frequencies that are significantly higher than those of the RadioAstron. From the engineering perspective, the Millimetron is a space telescope with a mirror 10 meters in diameter cooled to cryogenic temperatures, which will be launched to the Sun–Earth system's L2 libration point located at a distance of 1.5 mln km from Earth in the direction opposite to that to the Sun. The maximum distance from the ecliptic plane of the spacecraft moving in this orbit is 910,000 km, and its period in a reference frame corotating with Earth around the Sun is 180 days. The Millimetron observatory will be able to operate in two regimes: as a supersensitive 10-meter space telescope and as a space arm of a ground–space interferometer with a super-long baseline that will attain a uniquely high angular resolution. In other words, the 10-meter space telescope will perform observations of a particular source concurrently with one or more ground-based telescopes and ensure accurate referencing of observations to a time scale. To achieve this goal, unique hydrogen frequency standards with record-setting time stability and purity of the reference signal have been developed and produced for this project.

The sensitivity and resolving power of the Millimetron, RadioAstron, and EHT are compared in Figs 1 and 2. We note that a rather conservative range 211–275 GHz is used as the maximum frequencies observable by the Millimetron while, in principle, observations are possible at significantly higher frequencies of the order of 900 GHz. However, the sensitivity of the Millimetron at frequencies this high will probably be significantly lower than that shown in Fig. 1.

Figures 1 and 2 show that the Millimetron space observatory project is significantly superior to the other two projects. The Millimetron is superior to the RadioAstron regarding sensitivity and resolving power. A conceptual advantage is also its capacity to conduct observations at significantly higher frequencies because in the operational frequency range of the RadioAstron, the environment in the vicinity of SMBHs is, according to our current understanding, nontransparent due to synchrotron self-absorption and scattering on plasma irregularities. The Millimetron will operate in the same frequency range as the EHT and will feature a comparable sensitivity. However, its resolving power will be higher by a factor of approximately 50. Owing to this, it will be possible to both resolve a significantly larger number of space sources radiating in the millimeter waveband and observe sources resolvable by the EHT but in much greater detail. Below, as a rough estimate, we assume the Millimetron threshold sensitivity ($S_{\min}$) to be of the order of 1 mJy, and its resolving limit ($\theta_{\min}$) of the order of 0.1 ang. μs.

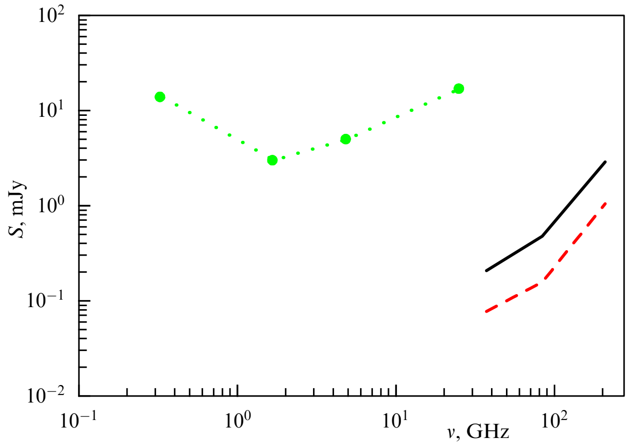

Figure 1. Sensitivity curves S of the Millimetron (solid curve), EHT (dashed curve) and RadioAstron (dotted curve) as functions of frequency. The sensitivity curve of the Millimetron in the VLBI regime is plotted on the Millimetron–ALMA base using the sensitivity calculator developed at the Astro Space Center of the Lebedev Physical Institute (see millimetron.radioastron.ru). The pass band width of the Millimetron receiver was adopted to be 4 GHz and the integration time 15–120 s. Dots on the RadioAstron sensitivity curve show positions of observational frequencies. ALMA and LMT were chosen here (as in Fig. 2) as the systems representing the EHT.

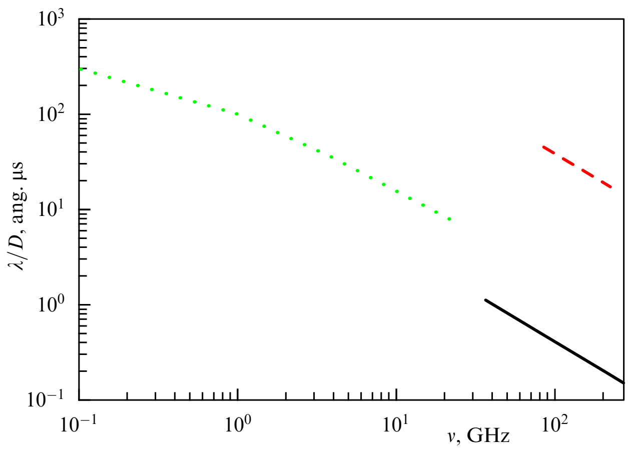

Figure 2. Resolving power of the Millimetron (solid curve), RadioAstron (dotted curve), and EHT (dashed curve) defined as the ratio of the observation wavelength and a characteristic size of the interferometer arm plotted as a function of observational frequency.

VLBI observations using the EHT and Millimetron (see [1]) will enable observing shadows of the SMBHs located in the centers of galaxies. Such observations will allow not only confirming that the black holes are the source of activities of various types in the galactic centers but also determining their masses and angular momenta. By observing the black hole shadows, it will be possible to independently test the general relativity (GR) theory in the so-called strong-field regime where the paradigm of Newton's classical gravitation theory is conceptually incorrect. It will also allow clarifying the nature of black hole activity associated with gas accretion and jet formation.

There is currently no universally adopted picture of how radiation is generated in the millimeter waveband in the spectra of SMBH candidates. Some authors assume that radiation of that kind is formed in jets, but in the opinion of others, it is generated, at least in some objects (for example, in the Galaxy center), directly in a geometrically thick accretion disk (or torus) surrounding black holes. It is quite possible that the region where the radiation is generated depends on the particular object. Future observations of the intensity distribution in the close vicinity of the event horizon will enable reliably resolving this issue and clarifying the nature of jet triggering, i.e., deciding whether jet formation is related to the so-called Blandford–Znajek mechanism, in which black hole rotation plays an important role, or it is caused by magnetohydrodynamic processes in the accretion disk. It will be possible, for some objects, to observe scales that are smaller than the event horizon and to understand the structure of accretion flows at short distances. This issue is of importance for understanding the nature of turbulence in the accretion disks, the central problem of the modern accretion theory.

The Millimetron operating in the VLBI regime will be able to resolve several dozen SMBHs located in the centers of the nearest galaxies, including ours. It will provide the ultimate evidence that black holes are the sources of activity in the centers of those galaxies, accurate measurements of their masses, and estimates of their angular momentum. Measurements of radiation polarization and intensity at the horizon and smaller scales will make it possible to determine which mechanism, accretion disk or jet, makes the main contribution to their luminosity and to shed light in this way on the nature of jets and turbulence in accretion disks.

In contrast to observations in the optical or, for example, X-ray range of the spectrum, VLBI observations usually fail to fully determine the spatial structure of the sources due to the incomplete filling of the $U-V$ plane, which, from the technical standpoint, is a 2D Fourier image of the source intensity distribution. VLBI observations can only determine intensities and phases of some spatial harmonics in the intensity distribution that are controlled by the distances between the telescopes involved in the realization of the space interferometer and orientation of the latter with respect to the direction to the source under study. Of special importance in this situation are various theoretical models that take other properties of the source into account, such as its spectrum at various wavelengths, variability, and SMBH mass estimates. It is for this reason that we pay significant attention to these models in this review.

The review is organized as follows. In Section 2, we present various theoretical models of accreting black holes and the generation of radiation in the millimeter waveband. Special attention is paid here to weakly accreting objects, because objects of this type are the main observation targets for both the EHT and Millimetron. In Section 3 we propose a simple criterion of how a particular source can be detected by an interferometric system similar to the EHT and Millimetron. It is based on fitting the numerical results for the distribution of radiation intensity of the black hole located in the center of the galaxy M 87 in the framework of an analytic model. In other words, this criterion assumes that all other possible sources are similar to M 87 but are located at other distances and differ only by the black hole mass and total radiation flux in the millimeter range. We have used observational data for the last three parameters and the values of the EHT and Millimetron observation baselines to compose a preliminary list of objects that, in our opinion, could be observed in those experiments. This list is shown in Section 3. Section 4 contains a discussion of the models we use and the conclusions made.

2. Theoretical models of accreting black holes: sources of radiation in the millimeter (submillimeter) range of the spectrum

2.1 Main features of accreting black hole candidates to be observed by the Millimetron

Using various methods, very massive objects have been identified in the centers of most galaxies, with their gravitational field coinciding with the field of a pointlike source whose mass is of the order of $10^5-10^{10} M_{\odot}$. These objects are apparently the sources of powerful electromagnetic radiation in a broad range from radio to X-ray waves; jets are also observed in some galactic centers.

The main features of these objects, i.e., the mass and characteristics of their radiation, enable us to assert rather confidently that they are black holes on which surrounding gas is accreting and which emit significant energy in the form of electromagnetic radiation and collimated particle flows, generated due to the gas rest mass deficit that emerges as a result of accretion. Therefore, although it would be more correct to refer to these objects as 'black hole candidates' until black holes in galactic centers are directly discovered, we nevertheless refer to them as SMBHs.

According to the simplest description of accretion, the most important role is played by the black hole mass and bolometric luminosity generated around it. It is convenient to represent bolometric luminosity in units of the so-called Eddington luminosity $L_{\rm Edd}$ defined as the luminosity ensuring the radiation pressure of the central source sufficient to prevent electron–proton plasma from falling onto the gravitating center. The formula for the Eddington luminosity can easily be deduced in the form

$$L_{\rm Edd} = 1.25 \times 10^{44} M_6 \ {\rm erg\,s^{-1}}\,, \qquad (1)$$

where $M_6 \equiv M/(10^6 M_{\odot})$. It is also convenient to define the mass flow to the black hole associated with the Eddington luminosity as $\dot{M}_{\rm Edd} = 10 L_{\rm Edd}/c^2$, where c is the speed of light. We note that the definition of the Eddington mass flow assumes that the expected energy release efficiency is 10%, a value typical of accretion in a thin accretion disk. Using Eqn (1), we obtain

$$\dot{M}_{\rm Edd} = 1.39 \times 10^{24} M_6 \ {\rm g\,s^{-1}}\,. \qquad (2)$$

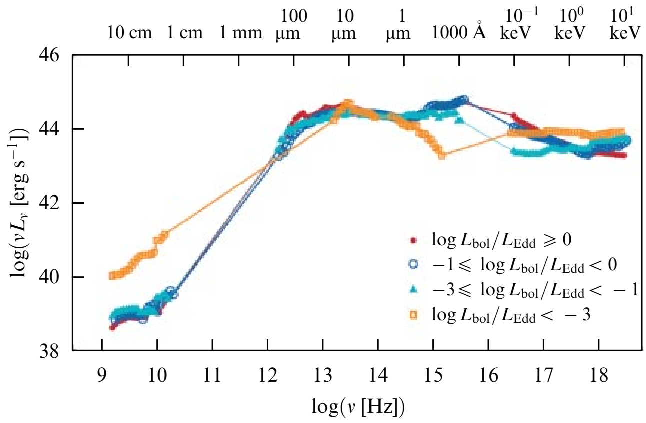

Figure 3. (Color online.) Averaged spectral radiation fluxes (per frequency logarithm unit) as a function of frequency for a group of objects with various values of the ratio $L_{\rm bol}/L_{\rm Edd}$. All radiation luminosities are normalized to the same value at a specific frequency. The red curve corresponds to $L_{\rm bol}/L_{\rm Edd} > 1$, dark blue to $0.1 < L_{\rm bol}/L_{\rm Edd} < 1$, light blue to $10^{-3} < L_{\rm bol}/L_{\rm Edd} < 0.1$, and brown to $L_{\rm bol}/L_{\rm Edd} < 10^{-3}$ (see [2]).

We introduce a useful dimensionless expression for the mass flow as the ratio of $\dot{M}$, the mass flow to the black hole, to its Eddington value, $\dot{m} = \dot{M}/\dot{M}_{\rm Edd}$.

For scales of the order of the gravitational radius to be successfully resolved, the observed objects should not be located very far away or should be very massive. Accreting black holes located at distances of the order of several dozen Mpc, in a relative vicinity of the Milky Way, have an important property: they are relatively weakly accreting objects whose typical ratio of the bolometric luminosity $L_{\rm bol}$ to its Eddington value is of the order of or less than 10^{-3}. Theoretical approaches assume that the character of accretion for such objects differs from that in the case of a standard thin accretion disk.[1] This assumption is confirmed by observations, as follows from Fig. 3, which shows averaged spectra of objects with various ratios of the bolometric and Eddington flows normalized at some frequency.

Figure 3 also shows that objects belonging to the $L_{\rm bol}/L_{\rm Edd} < 10^{-3}$ group have two specific features. First, they exhibit a significant power excess at low frequencies, which is usually interpreted as the emission of a jet. Second, there is no power excess in the ultraviolet (UV) range close to the 1000 Å wavelength (referred to as the Big Blue Bump), which is usually interpreted as a spectral signature of a thin accretion disk. However, an effective generation of jets and the absence of significant UV radiation can be reproduced within models of another type, which may be conventionally referred to as radiatively inefficient geometrically thick accretion disks, to be discussed in Section 2.2. Because these models are involved in interpreting SMBH observations in any VLBI explorations in the millimeter (submillimeter) wave band, their main features are of great importance for experiments of that kind.

2.2 Radiatively inefficient accretion flows

The main distinguishing feature of a radiatively inefficient accretion flow is that the plasma accreting on it is rather rarified and cannot be efficiently cooled owing to free–free transitions of electrons and synchrotron radiation. As a result, the main features of such an accretion flow are quite different from those of the 'standard' geometrically thin and optically thick accretion disk [4, 5]. Because plasma in the accretion flow is efficiently heated due to dissipation of the turbulent motion energy and the radiation cooling processes are ineffective, the disk extends in the vertical direction to a size of the order of the distance to the black hole, thus becoming geometrically thick. At the same time, as the disk half-thickness grows, pressure gradients in the horizontal direction become important, typically causing a decrease in the disk rotation velocity in comparison to its Kepler value. The increased half-thickness can also enhance the role of advective cooling. In other words, heat, instead of being transported away at a given radius by radiation, is 'entrained' by the radial flow towards the black hole. Therefore, the first models proposed for radiatively inefficient geometrically thick disks were referred to as advection dominated. Subsequently, it was found that other factors also determine the structure of rarified accretion disks: the possible occurrence of two temperatures in the plasma, outflows of accreting matter from a geometrically thick disk, convective motions, and possible advection toward the black hole and the growth of the poloidal magnetic field.

At the same time, a rarified radiatively inefficient disk can be optically thin in the millimeter (submillimeter) range of the spectrum, and the generation of millimeter (submillimeter) wavelength photons is primarily determined by synchrotron radiation of relativistic electrons (and possibly positrons) similar to jet radiation. As in a jet, the radiated electrons can exhibit both thermal and nonthermal distributions (usually approximated with a power-law function of energy) related, for example, to reconnections of magnetic field lines. A factor of utmost importance is that the disk luminosity in the millimeter (submillimeter) range of the spectrum can be comparable to or even exceed that of the jet. Therefore, studying accretion disks of this type is one of the most important problems in interpreting VLBI observations in the millimeter (submillimeter) range.

Another important feature of these disks is that they can be optically thin in the millimeter (submillimeter) range of the spectrum, which allows observing the vicinity of black holes using VLBI. Finally, the disk being geometrically thick facilitates the generation of strong magnetic fields required for initiating a jet and its collimation due to intense matter outflow (wind), which is very plausible in such a disk.

Many authors have studied radiatively inefficient accretion disks after their concept was proposed using analytic and numerical methods. The numerical approach prevailed because the disk models proved to be rather sophisticated for analytic treatment and rather simple for computations. However, the numerical methods feature a common disadvantage: their results, with a few exceptions where some qualitative conclusions can be drawn, cannot be generalized to other initial and boundary conditions and, in the case of complex models containing dimensional parameters, to other black hole masses. A circumstance additionally complicating relativistic calculations is that their results depend on the black hole rotation and disk orientation with respect to the equatorial plane.

Historically, the first theoretical approach was to use a model in which all values of interest were averaged over the vertical coordinate and assumed to be time independent (see, e.g., [6]). The main feature distinguishing that approach from the thin-disk models developed earlier was that it included

[1] Properties of 'standard' geometrically thin relativistic disks are described, for example, in [3].

radial advection of thermal energy in the heat transfer equation and radial pressure gradient in the Navier–Stokes equations. Generally speaking, these equations have also been solved numerically; however, self-similar solutions were found in [7]; for reference, we present their modified version with possible gas outflow taken into account (see also [8]):

$$v_r \approx 10^{10}\alpha r^{-1/2}\ [\mathrm{cm\ s^{-1}}],\quad \Omega \approx 3\times 10^{-2} M_6^{-1} r^{-3/2},$$
$$T \sim 10^{12} r^{-1}\ [\mathrm{K}], \tag{3}$$

$$n_{\mathrm{e}} \approx 6\times 10^{13}\alpha^{-1} M_6^{-1}\dot{m} r^{-3/2+s}\ [\mathrm{cm^{-3}}],$$
$$B \approx 6.5\times 10^{5}(1+\beta)^{-1/2} M_6^{-1/2}\dot{m}^{1/2} r^{-5/4+s/2}\ [\mathrm{G}], \tag{4}$$

where v_r is the gas velocity in the radial direction, Ω is the angular frequency of the azimuthal rotation of gas, T is the plasma temperature, n_{e} is the density of thermal electrons, B is the magnetic field, $r = R/R_{\mathrm{g}} = c^2 R/(2GM)$ is the ratio of the radial coordinate to gravitational radius, R is the radial coordinate, α is the Shakura–Sunyaev viscosity parameter, and $\beta = P_{\mathrm{gas}}/P_{\mathrm{magn}}$ is the ratio of the gas pressure to the magnetic field pressure. Typical values that follow from numerical calculations are $\beta \simeq 10$. The parameter s that takes the probability of outflow from the disk into account was introduced in [9] in a phenomenological way: it was assumed that the mass flow $\dot{M}(R)$ at a given radius R is related to the mass flow towards the black hole as $\dot{M}(R) = \dot{M}(R/R_{\mathrm{g}})^s$. Fitting parameters of radiatively inefficient models to observational data for specific sources (for example, the Galaxy center) yield a value $s \sim 0.3$, while the values in the numerical models are of the order of 0.4–0.8 (see, e.g., [10]).

The initial model of radiatively inefficient flows was based on some assumptions whose reliability was studied later within various analytic, numerical, and phenomenological models. In particular, in addition to the abovementioned possibility of outflows, which was explored within the models of so-called advection-dominated inflow–outflow solutions (ADIOSs), the following options have been explored:

(1) The possibility of formation of two-temperature plasma. This can happen because the dissipated energy of turbulent motions primarily heats protons, while the energy transfer from protons to electrons is suppressed in rarified plasma. There are currently arguments in favor of the possibility that a significant part of the energy, of the order of 50%, dissipates directly into the thermal energy of electrons (see the discussion in [8]);

(2) Flows can be controlled by convective motions, wherein the angular momentum outflow due to the work of viscous forces is almost compensated by the angular momentum flow related to motions of convective eddies. These solutions were called convective dominated accretion flows (CDAFs) (see, e.g., [11, 12]). The mass flow towards a black hole in these solutions turns out to be anomalously small, making them similar to the ADIOS models, which is apparently confirmed by observations;

(3) Luminous hot accretion flows (LHAFs) can emerge for relatively large $\dot{m}$. Radiative cooling in such flows prevails over the local heating; nevertheless, the disk remains geometrically thick due to the heating of matter as a result of compression in the process of moving toward the black hole (see the discussion in [8]);

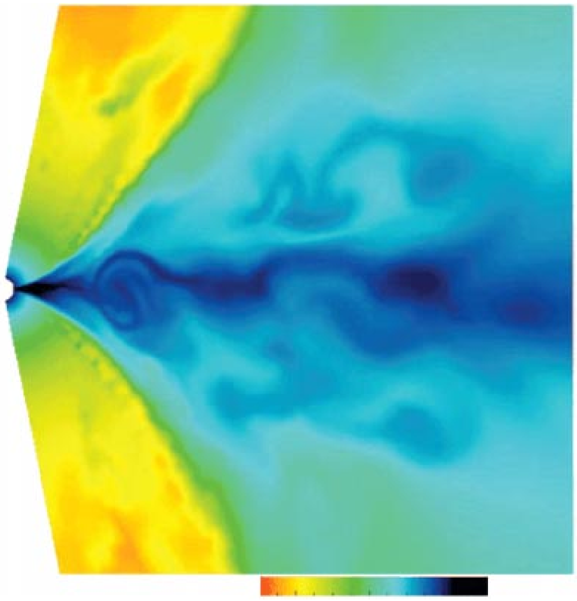

Figure 4. (Color online.) Matter density distribution in a numerical model of an accretion disk in the MAD regime. A disk cross section transverse to its plane is shown. (Taken from [16].)

(4) Magnetically arrested disks (MADs) can occur. These numerical solutions based on an analytic model proposed in [13, 14] appear if the system under consideration includes a strong poloidal magnetic field of nearly constant polarity frozen into plasma. This field is entrained by the accretion flow to the vicinity of the black hole and increases there to values that start affecting the character of plasma motion.[2] Because plasma cannot move across magnetic field lines in the case of ideal magnetohydrodynamics, accretion to black holes is suppressed in such solutions and only occurs via nonsymmetric streams of gas that emerge due to instabilities of a certain kind (Fig. 4). Strong quasistationary jets around a rotating black hole can emerge in such solutions. We note that for this regime to be valid, both special configurations in the distribution of the poloidal component of the magnetic field at long distances and a rather small magnetic diffusion coefficient (compared to the turbulent kinematic viscosity coefficient) are needed (see, e.g., [15]);

(5) Sometimes, a phenomenological model is used that assumes that the disk is geometrically thick only inside a radius r_{tr}, and becomes a standard thin disk beyond this radius. This model is used to describe the spectra of extragalactic sources, where an optical/ultraviolet radiation excess is observed; this phenomenon is interpreted as radiation of a thin disk that truncates at the transition radius r_{tr}. We note that this model resembles the well-known Shapiro–Lightman–Eardley (SLE) model (see [17]) that was successfully applied to the spectra of black hole candidates in binary stellar systems. A qualitative picture of that model is shown in Fig. 5. We note that this model is not sufficiently substantiated from the theoretical standpoint, and the transition radius is introduced as a phenomenological parameter.

One-dimensional models have been used to study not only the properties of unperturbed flows but also the problem of

[2] We note that the effects related to violation of the freezing-in condition can suppress the increase in the field (see, e.g., [15]).

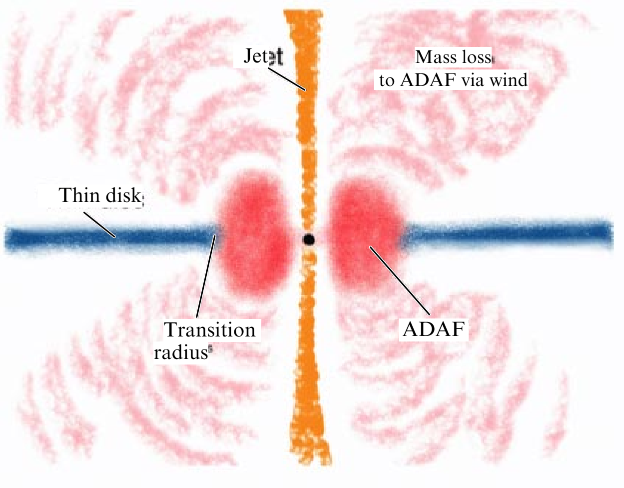

Figure 5. Quality image of the accretion disk cross section that changes from a thin disk at large radii to a thick one at small radii, along with a jet propagating perpendicular to the jet plane and the ADAF (advection dominated accretion flow) wind outflowing from the disk. (Taken from [18].)

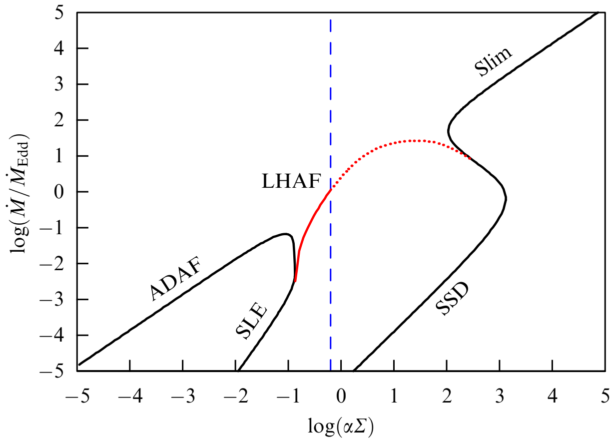

Figure 6. Logarithm of the ratio of mass flow to the Eddington value as a function of a product of the viscosity parameter α and the surface density Σ, plotted for various models of accretion disks: advection-dominated optically thin disk (ADAF), luminous hot accretion disk (LHAF), standard thin disk (SSD), advection-dominated optically thick disk (Slim), and the Shapiro–Lightman–Eardley model (SLE) solution. Calculations were performed for $\alpha = 0.1$, $r = 5$, and $M = 10M_\odot$. (Taken from [8].)

stability. All the main models turned out to be stable with respect to both thermal and viscous instabilities. This conclusion is illustrated in Fig. 6, where the values of $\dot m$ for solutions of various types are presented as a function of the Shakura–Sunyaev viscosity parameter α times the disk surface density Σ (at some radius). It can be seen that the solutions that correspond to both radiatively inefficient disks and the standard thin disk (and its natural generalization to the case of large mass flows, an optically thick advection-dominated (slim) disk) exhibit a positive slope of the mass flow vs. surface density dependence and are therefore stable with respect to viscous instability. However, the Shapiro–Lightman–Eardley solution is apparently unstable. We can also conclude from Fig. 6 that two stable solutions can exist in principle for a given low mass flow: the standard thin disk and the geometrically thick and optically thin advection-dominated disk. Which of these two solutions is realized is probably determined by the conditions of disk formation at large radii.

The energy release efficiency, defined as the ratio $\epsilon = L_{\rm bol}/(\dot M c^2)$, is shown in Fig. 7. We can see from Fig. 7 that if the mass flow is sufficiently large, the energy release efficiency becomes close to the nominal efficiency of the standard thin disk. We note, however, that because the calculations take the wind-driven mass loss into account, the energy release efficiency determined with respect to the mass flow at large distances always remains small.

One-dimensional models fail to provide answers to many of the most important questions of the accretion disk theory. First, it is impossible to determine the nature of turbulence in disks and therefore impossible to estimate the parameter α from first principles. Second, a solution containing jets, outflows, and convective motions cannot be obtained in a self-consistent way. Third, it is impossible to obtain accurate images of the disk and the black hole and the corresponding visibility amplitudes.

However, multidimensional numerical models are also plagued with some shortcomings. In particular, a numerical result obtained for specific initial and boundary conditions and parameter values is typically not suitable for general-

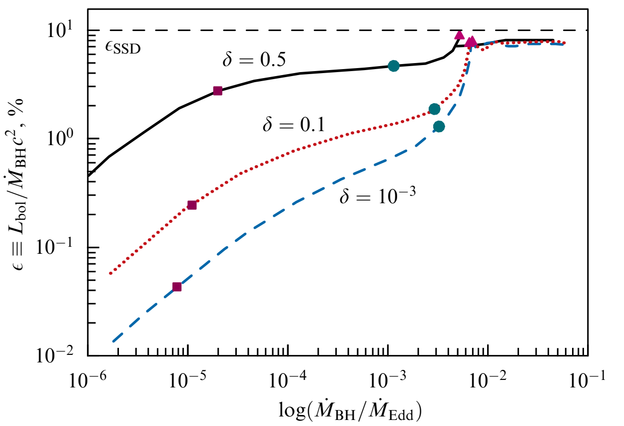

Figure 7. Energy release efficiency as a function of $\dot m$ for three values of the parameter δ that characterizes the fraction of energy transferred to electrons in turbulent motion dissipation, and $\alpha = 0.1$, $\beta = 9$, and $s = 0.4$. The curve with the constant value $\epsilon_{\rm SSD} = 10\%$ corresponds to the nominal energy release efficiency of the standard thin disk. If the flow mass is less than the values shown by squares, neither component, electronic or ionic, has enough time to emit energy during the accretion time. If the flow mass is smaller than that shown by dots, the ionic component alone releases energy. If the mass flow is less than the values shown by triangles, the bright hot disk regime occurs. (Taken from [19].)

izations to other conditions and parameters, especially in sufficiently complicated computational models containing dimensional parameters. A combined approach is needed in this situation, using the advantages of both analytic and numerical models, one-dimensional as well as multidimensional, and the phenomenological dependences obtained after performing a large number of numerical calculations.

Multidimensional numerical models have evolved from two-dimensional numerical schemes, used to compute hydrodynamic flows with a given viscosity law in a Newton (pseudo-Newton) potential, to three-dimensional general relativistic magnetohydrodynamics (GRMHD). An important specific feature of modern calculations of radiatively inefficient accretion disks is that in determining the dynamic and spatial structure of solutions, they do not usually take

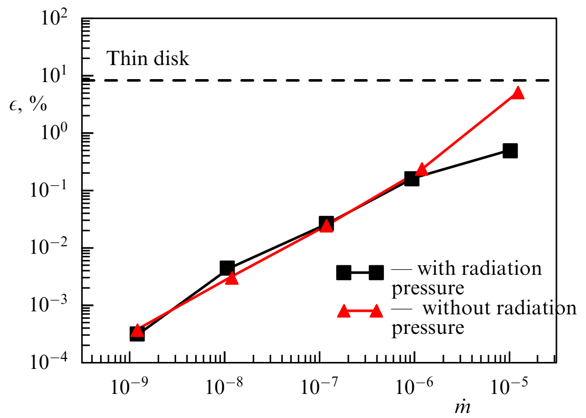

Figure 8. Energy release efficiency as a function of $\dot{m}$. The dashed horizontal line corresponds to the nominal efficiency of the standard thin disk. The black hole rotation parameter is $a = 0.5$ and $M = 10^8 M_{\odot}$. Triangles and squares are the results of respective calculations with and without taking the radiation pressure effect on the flow structure into account. (Taken from [20].)

radiation transfer into account, although several calculations have been published recently that do take this phenomenon into consideration (see, e.g., [20]). In calculating the spectra of objects and their images for various wavelengths, the radiation transfer equations are solved for given density and velocity fields and a certain magnetic field structure. We discuss the results of multidimensional numerical calculations in Sections 2.3 and 2.5; here, we only represent the dependence of energy release efficiency on $\dot{m}$ found numerically in fully relativistic models of two-temperature radiatively inefficient disks. Figure 8 shows that the multidimensional numerical schemes qualitatively confirm the dependence obtained using less sophisticated methods (see Fig. 7).

2.3 Theoretical models of relativistic jets

Spectra of many active nuclei of galaxies and quasars exhibit an excess of power in the radio-wave range, which is interpreted as synchrotron radiation in a jet of relativistic electrons (and, possibly, positrons) propagating from the black hole located in the source center. Such jets have been directly found in many sources using VLBI methods. It is generally believed that both the jet radiation and the formation of jets per se are related to the presence of magnetic fields in the jet and the accretion disk. A visualization of the black hole, accretion disk, and jet obtained in a numerical magnetohydrodynamic model is presented in Fig. 9.

A 'nucleus shift' effect is observed for jets resolved by VLBI (see, e.g., [22]): the angular dimension of the compact component of the jet located close to its visible base decreases as the frequency increases. This effect is interpreted as a decrease in the size of the optically thick jet region as the frequency increases. If the VLBI observations are performed in the millimeter (submillimeter) range, the angular size of the nuclei of many sources is supposed to become comparable to that of the gravitational radius, allowing us to hope that the region close to the black hole where the jet is formed can also be resolved. We note that this conclusion is confirmed by data on the radiation spectra of many active galactic nuclei and quasars that exhibit a break in the millimeter (submillimeter) range, which is explained as a transition, with increasing frequency, from an optically thick radiating environment to

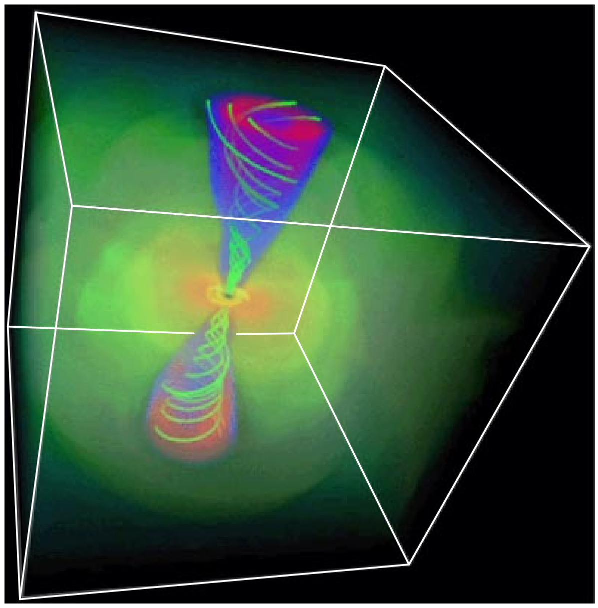

Figure 9. (Color online.) Accretion disk around a black hole and a jet outflowing perpendicular to the disk plane. The magnetic field lines in the jet shown as light curves are seen to have a spiral structure. (Taken from [21].)

an optically thin one. Therefore, it is expected for a large number of sources that the jet would be fully or partly optically thin in the millimeter (submillimeter) range, which is of utmost importance for the direct observation of the jet formation region in the VLBI regime.

There are a number of major problems related to the physics of jets. First, there is the problem of jet 'launch', which is believed to be directly related to the processes occurring in the accretion disk near the black hole. The second is the problem of jet collimation and the explanation of quasi-stationary and dynamic structures of various kinds that emerge in jets, such as 'knots' and the curved shape of jets on large scales. Third, there is a problem related to explaining the total jet power and formation of jet radiation, as well as polarization at various wavelengths and distances from the sources. There is also a related problem of jet composition: which jets — 'heavy' ones consisting mostly of protons and electrons or 'light' ones consisting mostly of electrons and positrons — primarily emerge in galactic centers. We emphasize that all these problems are closely related to each other, and currently there is no analytic or numerical theory that could explain main properties of the jets in a self-consistent way. It is for this reason that the VLBI observations of jets at various wavelengths are of utmost importance.

The most popular models of jet launch are based on either the Blandford–Payne model [23] or the Blandford–Znajek model [24]. In the first model, it is assumed that the matter outflowing from the accretion disk and moving along rotating poloidal magnetic field lines is accelerated under the effect of centrifugal force near the accretion disk and collimated at some distance from it owing to the presence of the poloidal component of the magnetic field. The second model, which is based on a certain similarity between the electrodynamic processes near the rotating black hole and a unipolar inductor, yields the following general picture: power is released near the black hole rotating in an external magnetic field whose field lines are perpendicular to the horizon, and the energy flow of the emerging electromagnetic field transports that power over long distances. We note that both models require the presence of the poloidal component of the magnetic field with a special configuration in the vicinity of the black hole, and, for the second model to be realized, the black hole must rotate.

Data on 'superluminal motion' of individual components indicate that the jet is accelerated at a distance from its source, acquiring a significant Lorentz factor $\Gamma \sim 10$. This implies that in the jet launch region where the Lorentz factor of outflowing matter is most probably not large, the energy flux must primarily occur in the form the Poynting flux and the plasma is supposed to be accelerated afterwards. A requirement of this kind can essentially be considered the definition of a relativistic jet, used in various numerical models of jet launches. These numerical models have shown that relativistic jets are most probably launched due to the Blandford–Znajek process, because their power strongly depends on the black hole rotation, in agreement with numerical results. We adopt this process as the main candidate for the role of the jet launching mechanism.

The power released due to the Blandford–Znajek process is given in its simplest form by the formula

$$L_{\mathrm{BZ}} = \frac{1}{32}\, a^2 \omega_{\mathrm{F}}^2 B_{\perp}^2 R_{\mathrm{h}}^2 c\,, \tag{5}$$

where a is the black hole rotation parameter, $\omega_{\mathrm{F}} = \sqrt{(\Omega_{\mathrm{h}} - \Omega_{\mathrm{F}})/\Omega_{\mathrm{F}}}$, Ω_{F} is the angular velocity of magnetic field line rotation, Ω_{h} is the angular velocity of black hole rotation, $B_{\perp}$ is the magnetic field component perpendicular to the horizon, and R_{h} is the event horizon radius (see, e.g., [25]). Assuming that $B_{\perp} \sim \alpha P$ (P is the pressure in the disk) in the vicinity of the black hole and using equations from [7] while also setting $\omega_{\mathrm{F}} \sim 1/2$, we can estimate the efficiency of energy release due to the Blandford–Znajek process (see [26]) in a radiatively inefficient disk:

$$\epsilon_{\mathrm{BZ}} \equiv \frac{L_{\mathrm{BZ}}}{\dot{M} c^2} \sim 10^{-2} a^2\,. \tag{6}$$

Comparing (6) with the efficiency $\bar{\epsilon}$ of energy release by the accretion disk itself (see Fig. 7), we see that the jet can be a more efficient energy source than the disk if the rotation parameter is large, $|a| \sim 1$, and the ratio of the mass flow to the Eddington flow is rather small, $\dot{m} < 10^{-5} - 10^{-3}$, depending on the efficiency of heating of electrons in the disk due to dissipation of turbulent motions. We note that estimates for both ϵ_{BZ} and $\bar{\epsilon}$ contain the value of the mass flow directly onto the black hole. As was noted above, the mass flow at much longer distances can be several orders of magnitude larger owing to possible strong mass outflows in radiatively inefficient disks. We emphasize that L_{BZ} provides only an upper bound for the radiation flow emitted from the jet and, moreover, there are reasons to expect that the radiation flow is much smaller than L_{BZ}. For example, the energy flow L_{jet} in the jet located in the central part of the galaxy M 87 can be estimated at long distances from its source by considering interaction of the matter flow in the jet with either the knots it contains (see [27]) or the intergalactic environment (see [28]). Estimates of this kind yield $L_{\mathrm{jet}} \approx 1.4 \times 10^{-4} L_{\mathrm{Edd}} \sim 10^{44}$ erg s^{-1} and $L_{\mathrm{jet}} \approx 4 \times 10^{-5} L_{\mathrm{Edd}} \sim 3 \times 10^{43}$ erg s^{-1}, the values that are significantly larger than the bolometric radiation luminosity from the center of that galaxy $L_{\mathrm{bol}} = 3.6 \times 10^{-6} L_{\mathrm{Edd}} \approx 2.7 \times 10^{42}$ erg s^{-1}. Evidently, $L_{\mathrm{jet}} < L_{\mathrm{BZ}}$.

At the same time, the radiation flux in the millimeter range, which is of interest to us, L_{mm}, is somewhat smaller than the bolometric flux (see, e.g., [29]). Therefore, the efficiency of the radiation energy release of the M 87 jet in the millimeter range is relatively small, even if the assumption is made that the M 87 spectrum in this range is fully determined by the jet.

It is believed that jets are collimated at long distances from the source owing to either the compressing effect of the magnetic field in the jet or the jet interaction with the environment. If the Lorentz factor of matter is sufficiently large and the 'effective' speed of sound in the jet is small (this value takes the pressure of both particles and the magnetic field into account), the relativistic Mach number is large: $\mathrm{M} \equiv \Gamma v_{\mathrm{j}}/c_{\mathrm{s}}$, where v_{j} is the characteristic velocity of particle motion in the jet and c_{s} is the effective speed of sound. The jet can also be collimated in this case purely kinematically, with the opening angle θ of the order of M^{-1} (see [30]).

Analytic theories of jet propagation typically address stationary axially symmetric configurations within ideal magnetohydrodynamics, where magnetic field lines are assumed to be frozen into plasma. In this approach, it is possible to find integrals of motion and derive an equation that controls magnetic field configurations and the distributions of particle density and velocity fields (the so-called Grad–Shafranov equation; see a review of the results obtained in that approach in [31]). It is not infrequent that to simplify the general equation, the so-called force-free approximation is used, in which the effect of the inertia force and pressure on the motion of matter is disregarded. Nonstationary solutions in the analytic theory are usually found by the perturbation theory and mainly pertain to the problem of stationary flow stability (see, e.g., [32]).

Unfortunately, ideal magnetohydrodynamics does not allow studying the generation of nonthermal particles or radiation in a jet; methods of kinetic theory must be used to determine these quantities. It is also probable that these processes are related to either reconnection of magnetic lines or propagation of shockwaves in the jet, and therefore have an essentially nonstationary nature. To calculate jet spectra, phenomenological 'quasi-hydrodynamic' models have been proposed (see, e.g., [33–35]), wherein it is assumed that the energy density of a radiating particle is proportional to the magnetic field energy density, and their energy distribution is described by a power law.

The main characteristics of a jet, such as typical values of Γ, θ, mass and energy flows in the jet, and the exponent of the power-law energy spectrum of radiating particles, are the parameters of the phenomenological models described above. They are determined by either fitting the model spectra to observations or employing other data on jets in specific sources. Of importance for VLBI observations in the millimeter range is that these phenomenological models frequently use a characteristic distance from the black hole at which initial acceleration of radiating particles to relativistic energies occurs; this distance is usually assumed to be several units or tens of the gravitational radius (the 'nozzle' or 'jet base' size). VLBI observations in the millimeter range will enable resolving the region around the black hole of the order of a characteristic jet base size and understanding both how the jet is formed and how radiating particles can be generated.

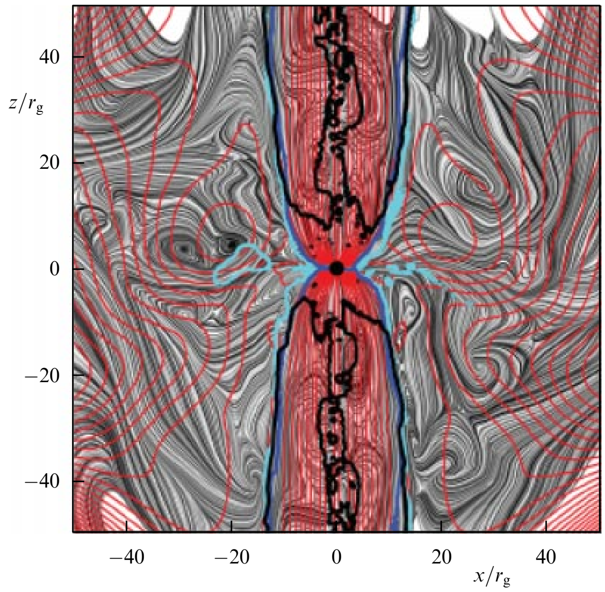

Figure 10. (Color online.) Projection of flow lines (grey lines) and magnetic field lines onto a plane perpendicular to the equatorial plane of a rapidly rotating black hole, in a numerical simulation of the emergence of a jet. Additionally shown are the regions within which gas elements have negative binding energy with respect to the black hole (black lines). Light blue lines correspond to the ratio of the gas pressure to the magnetic pressure less than 2, and dark blue to the ratio of the magnetic field density to the rest energy density greater than 1. (Taken from [37].)

Currently, numerical methods based on fully relativistic ideal magnetohydrodynamics are the main tool for studying the emergence of jets (see a review of studies in this area in [36]). For illustration, we present several images taken from [37]. Flow lines and magnetic field lines are shown in Fig. 10 for a model of an accretion disk that evolves in the regime of the dominating effect of the magnetic field (as opposed to gas pressure) on the motion of matter near the black hole (in the MAD regime) with a predominantly poloidal initial distribution of the magnetic field. It can be seen in Fig. 10 that a pronounced jet occurs in this case perpendicular to the disk plane, the density of the magnetic field energy in the jet exceeding that of the gas rest energy. As follows from Fig. 11, which also shows the gas density distribution in the same model, this distribution is nonsymmetric.

Figure 12 shows the gas density distribution in a model with a predominantly toroidal distribution of the magnetic field at the moment when a transient jet emerges.

As a whole, it was noted in [37] and other studies that for a pronounced quasistationary jet to form, a large value of the black hole rotation parameter, $a \sim 1$, and a predominantly poloidal distribution of the initial magnetic field are needed. As noted above, the latter requirement may not be satisfied in reality, either because of other initial conditions or due to the effects of magnetic field diffusion, that can hardly be taken into account in computations. An interesting model has been proposed recently in which a large-scale magnetic field is generated directly near the black hole (see [38]) due to the effect of the difference between rotation of the disk and that of the black hole on the magnetic field line loop. This model is apparently more effective if the disk rotates in the direction opposite to that of the black hole, while their rotation in the same direction seems to be more natural.

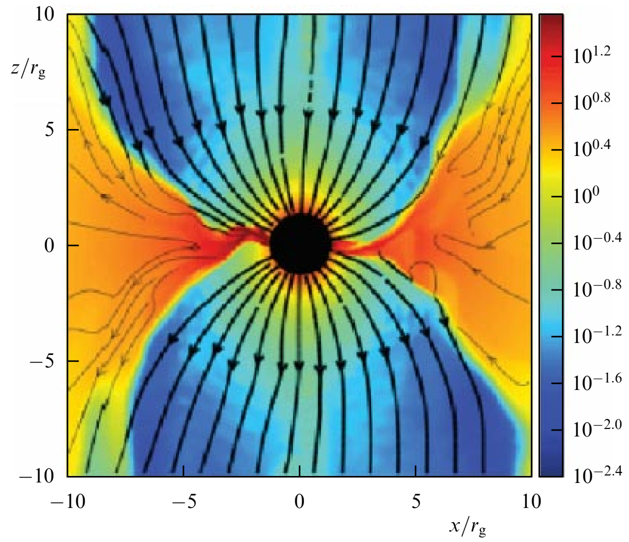

Figure 11. (Color online.) The same as in Fig. 10; however, here, highlighted in color is the distribution of the decimal logarithm of density measured in natural geometrical units of density. Black curves show the distribution of magnetic field lines, thick curves correspond to 'lightly loaded' field lines within which the magnetic field is strong enough for force-free magnetosphere to be created. (Taken from [37].)

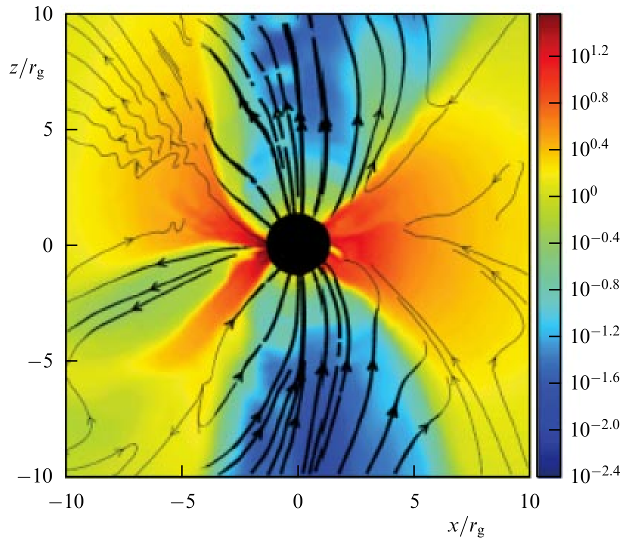

Figure 12. (Color online.) The same as in Fig. 11 but for a disk model with a 'normal' evolution, wherein gas motion near the black hole is primarily driven by pressure and gravitation. (Taken from [37].)

As was shown using analytic methods in [39, 40] and numerical approaches, e.g., in [41, 42], if the accretion disk is sufficiently thick and rotates in the same sense as the black hole does, it does not align with the black hole's equatorial plane at short distances from it when it is inclined with respect to that plane at long distances. In relation to this, the problem of the jet axis orientation becomes important.

A numerical model of the accretion torus inclined with respect to the black hole's equatorial plane and precessing around its rotation axis under the effect of the gravimagnetic force was used in a recent study [43] to show that the jet is oriented at sufficiently long distances perpendicular to the torus plane (Fig. 13). If this effect is confirmed in other models, it may prove to be of importance for constructing images of black holes, because all the available calculations of

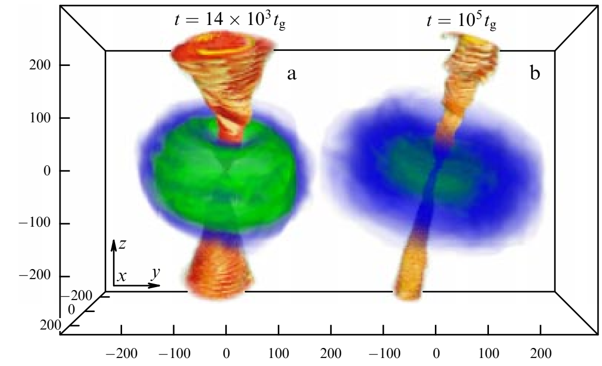

Figure 13. (Color online.) Visualization of numerical calculations of a system consisting of an accretion torus and a jet tilted with respect to the equatorial plane of a black hole for time values (a) $t = 14 \times 10^3 t_g$ and (b) $t = 10^5 t_g$, where t_g is the 'gravitational time' defined as the ratio of the gravitational radius t_g to the speed of light. Shown in green and blue is the logarithm of density in characteristic units; the green corresponds to larger density. Shown in red and yellow are magnetic field lines. (Taken from [37].)

this kind assume the standard configuration, with the disk being aligned with the equatorial plane and the jet directed perpendicular to it.

2.4 Simulating spectra of sub-Eddington luminosity radiation sources

Both the accretion disk and the jet can make comparable contributions to the radiation flow at millimeter (submillimeter) wavelengths in the case of sources with a small ratio of bolometric to Eddington luminosities. Moreover, the radiation flux in this region can determine the total source luminosity. A question arises: can a conclusion be made based on data on the radiation flux distribution as to whether the luminosity of a specific object is dominated by the jet or the disk? An attempt to answer this question has been made in [18] for a set of low-luminosity active galactic nuclei (LLAGNs), which are characterized by a low-ionization nuclear emission region (LINER). This set of objects is shown in Table 1, where some of their characteristics are also displayed. The study only focused on sources with a very low ratio of bolometric to Eddington luminosity of the order of 10^{-5}.

To simulate the accretion disk spectrum, model 5 is Section 2.2 was used, which assumes that the region inside the radius r_{tr} contains a radiatively inefficient optically thin and geometrically thick disk, while outside this radius the disk is standard, optically thick, and geometrically thin. The accretion flow structure in the region $r < r_{tr}$ was found numerically using the equations derived in [44]; the approach also takes possible mass outflow from the disk into account, characterized by the parameter s (see Section 2.2). It was assumed that the energy fraction δ directly dissipated into the heating of electrons is in the range $0.01 \leqslant \delta \leqslant 0.50$. It was also assumed that the thin disk emits black-body radiation. The set of other parameters that characterize the accretion disk includes r_{tr}, the viscosity parameter α, the ratio β of gas to magnetic pressure, the adiabatic index γ, the disk inclination angle with respect to the line of sight i, and the mass flow at the transition radius $\dot{M}(r_{tr})$, some of the values being fixed as $\alpha = 0.3$, $\beta = 10$, and $\gamma = 1.5$.

To model the jet spectrum, a quasi-hydrodynamic model was used that was initially proposed in [34] to simulate gamma-burst spectra. It was assumed that the jet is characterized by the constant opening angle $\theta = 10°$ and the gamma factor $\Gamma = 2.3$, while the jet inclination angle was either taken from observations or set equal to 30°. The fraction of nonthermal electrons was set to 10% of the thermal particle number density. The set of free parameters consisted of the mass flow in the jet, the energy densities of thermal particles and the magnetic field, and the parameter p that characterizes the energy distribution of nonthermal particles. We can see from Table 2, which displays the simulation results, that the obtained values of the parameters are realistic, and source radiation in this model is primarily determined by the jet in six cases, and by the accretion disk in eleven cases.

Simulated results of the spectral distribution of radiation flow are shown in Figs 14–16. Figure 14 displays the simulation results for two objects, NGC 3013 and NGC 3998. We can see that the models in which accretion disk radiation dominates yield a well-pronounced peak of radiation in the submillimeter region for those objects. The models where jet radiation dominates yield a less steep spectrum.

Figures 15 and 16 show the geometrical mean of spectra of various sources and its dispersion; they also show a comparison of the geometrical mean with the spectra of radio quiet and radio loud quasars. Similarly to the case of specific sources, the models wherein disk radiation dominates yield a spectrum with a well-pronounced maximum at submillimeter wavelengths. Both cases, disk and jet domination, exhibit a dip in the spectrum at wavelengths over 1 mm, apparently related to the optically thick regime of radiation propagation

Table 1. Sources whose spectra* have been simulated in [18].

Galaxy	Type	Distance, Mpc	lg $(M_{BH}/M_\odot)$	L_X, erg s^{-1}	L_{bol}, erg s^{-1}	L_{bol}/L_{Edd}
NGC 1097	SB(rl)b	14.5	8.1	4.3×10^{40}	8.5×10^{41}	5×10^{-5}
NGC 3031 (M 81)	SA(s)ab	3.6	7.8	1.9×10^{40}	2.1×10^{41}	3×10^{-5}
NGC 3998	SA(r)0	13.1	8.9	4.6×10^{41}	1.4×10^{43}	1×10^{-4}
NGC 4143	SAB(s)0	14.8	8.3	1.1×10^{40}	3.2×10^{41}	1×10^{-5}
NGC 4261	E2-3	31.6	8.7	1.0×10^{41}	6.8×10^{41}	1×10^{-5}
NGC 4278	E1-2	14.9	8.6	9.1×10^{39}	2.7×10^{41}	5×10^{-6}
NGC 4374 (M 84)	E1	17.1	8.9	3.5×10^{39}	5.0×10^{41}	5×10^{-6}
NGC 4486 (M 87)	E0-1	14.9	9.8	1.6×10^{40}	9.8×10^{41}	7×10^{-6}
NGC 4552 (M 89)	E	14.3	8.2	2.6×10^{39}	7.8×10^{40}	4×10^{-6}
NGC 4579 (M 58)	SAB(rS)b	21.0	7.8	1.8×10^{41}	1.0×10^{42}	1×10^{-4}
NGC 4594 (M 104)	SA(s)a	9.1	8.5	1.6×10^{40}	4.8×10^{41}	1×10^{-5}
NGC 4736 (M 94)	(R)SA(r)ab	4.8	7.1	5.9×10^{38}	1.8×10^{40}	1×10^{-5}

* M_{BH} is the black hole mass, L_X is the luminosity of the source in the range 2–10 keV.

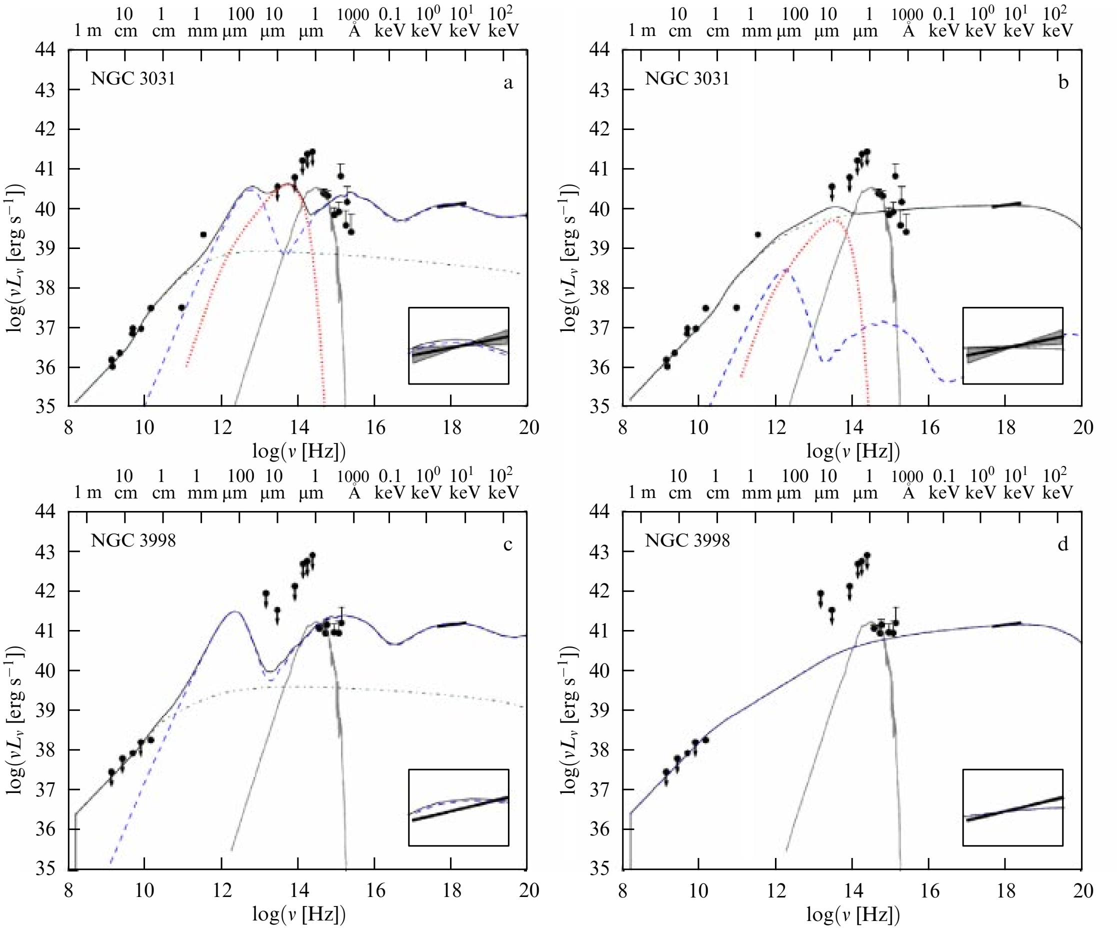

Figure 14. Spectral density distribution of radiation energy per unit of the logarithm of frequency as a function of the logarithm of frequency. The results of modeling (a, b) NGC 3031 and (c, d) NGC 3998 are shown. Results of the models where disk and jet radiation dominates are respectively displayed in (a, c) and (b, d). Dashed, dotted, and dashed-dotted lines show the respective spectra of a radiatively inefficient disk, a thin disk, and a jet. Symbols show the observed values of the flux and upper bounds for them at various frequencies. The solid black curve represents the total radiation density, and the solid grey line shows an additional component related to radiation of an old star subsystem. The insets display the X-ray part of the spectrum in the range 2–10 keV.

Table 2. Main results of simulations of the source spectra* from the set (taken from [18]).

Galaxy	Type**	$\dot{M}_0/\dot{M}_{\rm Edd}$	$r_{\rm tr}/R_{\rm Sch}$	$\dot{M}_{\rm jet}/\dot{M}_{\rm Edd}$	$P_{\rm jet}^{\rm mod}$, erg s^{-1}	$P_{\rm jet}^{\rm obs}$, erg s^{-1}	$\dot{M}_{\rm Bondi}/\dot{M}_{\rm Edd}$
NGC 1097	AD	0.0064	225	7×10^{-7}	10^{43}		
NGC 3031	JD	0.0005	360	1.2×10^{-5}	4.8×10^{42}	7.1×10^{41}	
NGC 3031	AD	0.004	360	2×10^{-6}	8×10^{41}		
NGC 3998	JD	—	—	3.5×10^{-6}	1.8×10^{43}	4.6×10^{42}	
NGC 3998	AD	0.006	10^4	1.7×10^{-6}	9×10^{42}		
NGC 4143	AD	0.0025	70	1.2×10^{-7}	1.6×10^{41}		
NGC 4261	AD	0.0019	10^4	6×10^{-6}	2×10^{43}		
NGC 4278	AD	0.0007	40	3.5×10^{-6}	4×10^{42}		
NGC 4374	JD	—	—	1.6×10^{-6}	8.4×10^{42}	3.9×10^{42}	
NGC 4374	AD	0.0029	10^4	4×10^{-7}	2×10^{42}		
NGC 4486	JD	—	—	6×10^{-8}	8.2×10^{42}	$10^{43} - 10^{44}$	7×10^{44}
NGC 4486	AD	0.00055	10^4	5×10^{-8}	6.8×10^{42}		
NGC 4552	JD	—	—	1.8×10^{-6}	2.2×10^{42}	1.6×10^{42}	
NGC 4579	AD	0.02	150	$1.4 \times .10^{-5}$	5.9×10^{42}		
NGC 4594	JD	0.002	10^4	4.5×10^{-7}	10^{42}	3×10^{42}	
NGC 4594	AD	0.006	10^4	9×10^{-7}	2×10^{42}		
NGC 4736	AD	0.0035	60	6×10^{-7}	6.5×10^{42}		

* $\dot{M}_0$ is the accretion flow at the transition radius $r_{\rm tr}$, $\dot{M}_{\rm Edd}$ is the Eddington flow, $R_{\rm Sch}$ is the Schwarzschild radius, $\dot{M}_{\rm jet}$ is the mass flow in the jet, $P_{\rm jet}^{\rm mod}$ is the total jet power, $P_{\rm jet}^{\rm obs}$ is the estimated total jet power found from observations (if available), and $\dot{M}_{\rm Bondi}$ is the observational estimate of the mass flow at the black hole's Bondi radius.

** AD means that luminosity is determined by disk radiation, and JD, by jet radiation.

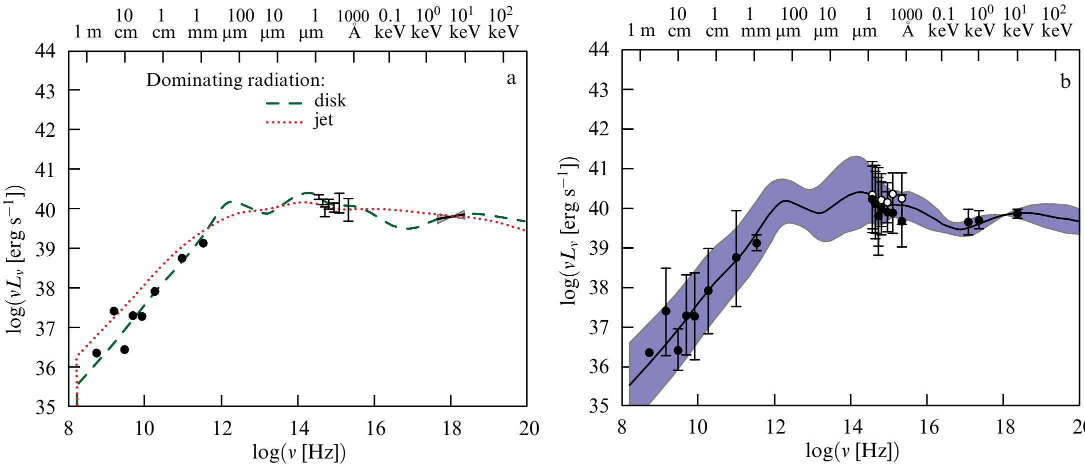

Figure 15. The same as in Fig. 14, with (a) the geometrical mean of spectrum models of individual sources and observational data and (b) the standard deviation. The respective dashed and dotted lines in (a) correspond to models where the disk or jet radiation dominates.

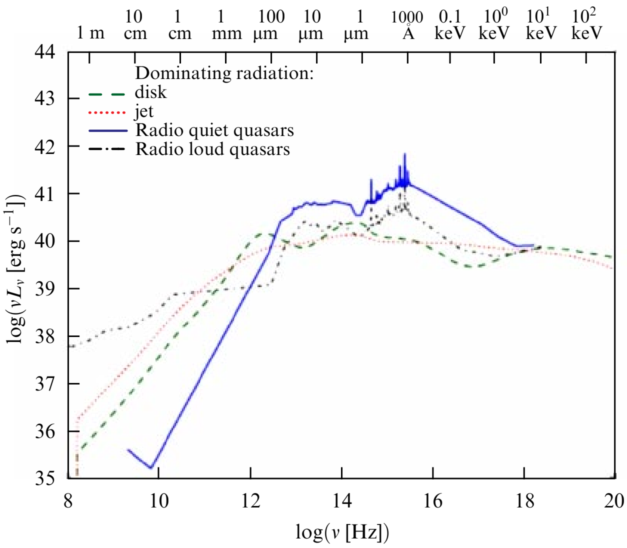

Figure 16. The same as in Fig. 14; dashed, dotted, solid, and dashed-dotted curves respectively correspond to the averaged spectra obtained in models in which disk radiation (AD_{mean}) or jet radiation (JD_{mean}) dominates and to averaged observation spectra of radio quiet and radio loud quasars. All spectra are normalized to the same value in the energy range 2–10 keV.

in radiating plasma for rather long wavelengths. We can see from Fig. 16 that the radiation flow maximum of a 'typical' quasar is shifted towards shorter wavelengths compared to that of active nuclei with weak bolometric luminosity.

Summarizing, the results of the study show that there is a significant difference between the spectra of quasars and low-luminosity active galactic nuclei. It can be expected in the latter case that a significant part of the total luminosity is emitted in the range 100 μm – 1 mm. The contribution of the accretion disk to the radiation power in the specified range may also be significant in the latter case. We note, however, that this conclusion must be confirmed by more realistic models of radiation formation in disks and jets.

2.5 Black hole shadows

The trajectories of photons weakly interacting with matter that pass close to black holes are heavily distorted by their gravitation field. Moreover, photons moving in orbits with a sufficiently small angular momentum (whose value depends, generally speaking, on the black hole angular momentum and orientation of that orbit with respect to the black hole rotation axis) are absorbed by the black hole. As a result, a black hole illuminated by some source looks (at long distances) like a black spot whose angular size is of the order of several units of the ratio of the gravitational radius to the distance to the black hole, while the shape of the spot depends on the properties of the radiation field source, the angular momentum of the black hole, and the orientation of its rotation axis with respect to the direction to the observer (see, e.g., [45, 46]). This spot is referred to as the black hole 'shadow'; discovering that shadow would be direct evidence that a particular galaxy contains a black hole. Moreover, the spot shape enables making some conclusions regarding the black hole's mass, its angular momentum, and orientation with respect to the line of sight. Some information can be obtained about the properties of the radiating environment and the extent to which the GR theory is valid in strong gravitational fields. Because angular dimensions of the shadows of even SMBHs are of the order of several tens of millionths of an angular second or less, they can only be discovered using the VLBI technique, the most important role being played by VLBI observations in the millimeter range.

For the black hole shadow to be formed in a source image in a realistic situation, the radiating environment in the black hole's vicinity must either be optically thin or occupy a solid angle of less than 4π, the line of sight in the latter case being oriented toward the black hole in the direction along which there is no environment. The former situation seems to be realized in the case of radiatively inefficient accretion disks, while the latter situation occurs in the case of thin disks and jets if the line of sight does not lie in the disk plane or is not oriented along the direction to the jet 'funnel'.

Black hole shadows have been actively explored as part of the preparation for observations with the EHT[3]; unfortunately, only two sources have been studied in detail: the Galaxy center (Sgr A^*) and the center of the galaxy M 87. Despite the difference between the distances to these sources and black hole masses (several million solar masses in the former case and several billion in the latter), the angular dimensions of the shadows of both black holes are compar-

[3] See eventhorizontelescope.org/.

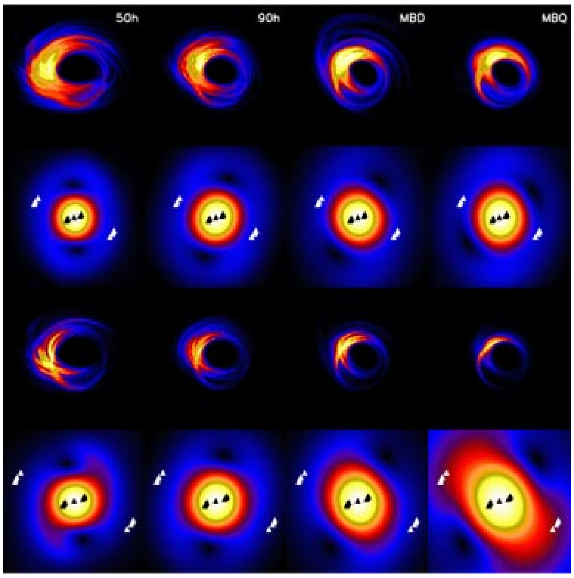

Figure 17. Accretion disk images obtained in computations with the parameters that correspond to the black hole in the Galaxy center (first and third rows of the images) and the corresponding visibility amplitudes (second and fourth rows of the images). The first two rows correspond to the wavelength 1.3 mm, and the last two, to 0.87 mm. Triangles show the location of observational bases in [47]. Each column corresponds to an individual computation. (Taken from [48].)

able by the order of magnitude and make several dozen angular microseconds. However, all characteristics of the sources that have been determined by now can be explained in the former case by the presence of a radiatively inefficient disk alone, while a strong jet outgoing from the galaxy center can be observed in the latter case. Consequently, most of the Sgr A* models only consider the accretion disk, while the M 87* models assume that either jet radiation dominates or contributions from the jet and disk are comparable.

Because the VLBI methods can only provide so-called visibility functions (Fourier images of the source on the celestial sphere), often determined together with the black hole shadows are visibility amplitudes, i.e., the absolute values of the Fourier image of the inner part of the source that contains the black hole shadow.

The black hole shadows and the corresponding visibility amplitudes were usually found numerically using methods of fully relativistic magnetohydrodynamics and radiation transfer; first, magnetohydrodynamic computations were performed, followed by solving the radiation transfer problem for given metric and radiating environment properties.

Examples of black hole shadows and visibility function amplitudes are shown in Figs 17, 22, and 23 for Sgr A* and in Figs 18, 19, and 21 for M 87*.

An example of numerical calculations of accretion disk images in the vicinity of the black holes located in the Galaxy center (taken from [48]) is presented in Figs 3 and 17. The main parameters of the accretion model were chosen in [48] such that they correctly describe both data on the spectral distribution of radiation flux in the millimeter waveband and data from VLBI observations of the Galaxy center (available by 2010). We can see that, generally speaking, the shape of the black hole shadow depends on both its rotation parameter and the ratio of the temperatures of ions $T_{\rm i}$ to electrons $T_{\rm e}$. In particular, the computation whose results are displayed in the first column of images in Fig. 17, was performed for a rotation

Table 3. Main parameters used in numerical calculations [48].

Model name	Rotation parameter a	Mass flow $\dot{M}$, $10^{-9}\,M_\odot$ year^{-1}	Disk inclination angle with respect to the line of sight i, deg	$T_{\rm i}/T_{\rm e}$
50h	0.50	20–40	60	1
90h	0.90	5–8	50	2
MBD	0.92	4–10	50	3
MBQ	0.94	5–8	50	6

parameter value much smaller than in other computations. It can be seen that the area of the black hole shadow is larger in this case. Therefore, in principle, the shadow size can be used to make certain conclusions about black hole rotation if its mass is reliably determined. Computation parameters [48] used in various models are displayed in Table 3.

Examples of expected black hole shadows with parameters that correspond to the black hole in the center of M 87 are shown in Figs 18 and 19 (see [49]). Two models were used that differ by the $T_{\rm i}/T_{\rm e}$ ratio; in the model where $T_{\rm i}/T_{\rm e} = 3$, the expected image of the system is formed by radiation of both the jet and the disk, while in the model where $T_{\rm i}/T_{\rm e} = 10$, the jet alone is of importance. Figure 18 shows the expected images of the disk and jet and the corresponding visibility amplitudes for the expected relatively small angle of jet inclination with respect to the line of sight equal to 25°. The jet image is determined in this case by radiation from the counter-jet, because the jet radiation

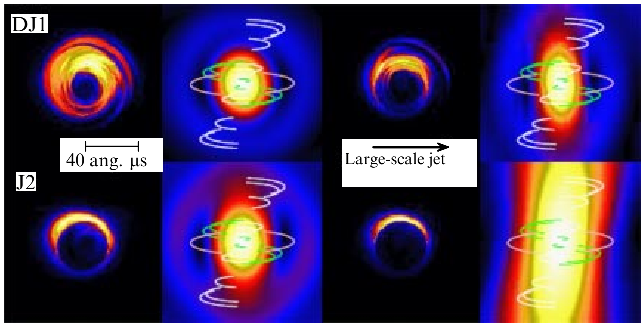

Figure 18. Disk and jet images (first and third columns) and visibility amplitudes (second and fourth columns) obtained in computations of an accreting black hole with the parameters that correspond to the black hole in the galaxy M 87 (Table 4). The lines in the visibility amplitude images correspond to the projections of the bases accessible in the EHT project. The first row shows the results of a model where the contributions of disk and counterjet radiation are important, and the second row shows those of the counter-jet alone. The first and second columns are calculated for a wavelength of 1.3 mm, and the third and fourth columns for a wavelength of 0.87 mm. (Taken from [49].)

Table 4. Main parameters* of the numerical models used in [49].

Model name	$T_{\rm i}/T_{\rm e}$	Mass flow $\dot{m}$, 10^{-4}	$\gamma_{\min}$	p	η
DJ1	3	1	50	3.25	0.05
J2	10	1	50	3.50	0.10

* $T_{\rm i}/T_{\rm e}$ is the ratio of ion to electron temperatures, $\dot{m}$ is the mass flow in units of the Eddington flow for a black hole with the mass $6.4 \times 10^9\,M_\odot$, $\gamma_{\min}$ is the minimum Lorentz factor of nonthermal electrons, p is the exponent in the energy distribution of nonthermal electrons, and η is the ratio of fractions of nonthermal to thermal electrons.

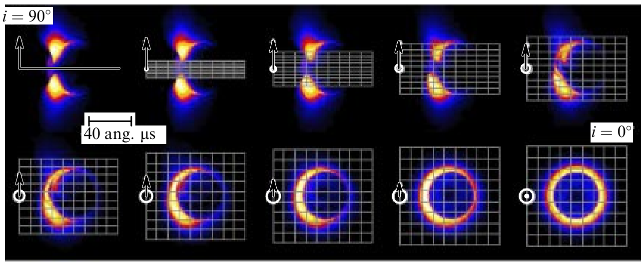

Figure 19. (Color online.) Jet image depending on its orientation with respect to the line of sight. The upper leftmost image corresponds to the line of sight perpendicular to the jet axis, and the lower rightmost image to the line of sight parallel to the jet axis. Arrows show how the angular momentum of the black hole (and the jet) is oriented with respect to the line of sight. (Taken from [49].)

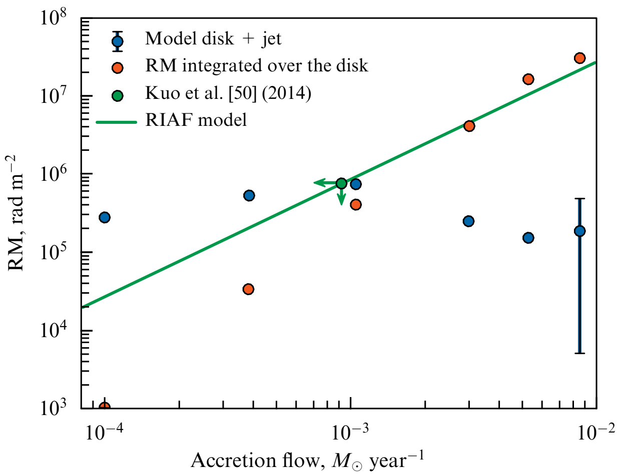

Figure 20. (Color online.) Rotation measure (RM) values obtained in various numerical models of the disk and the jet in the galaxy M 87 as a function of mass flow. Dots correspond to various numerical models, and the dot with arrows shows the observational constraint from [50]; the line is plotted for a semi-analytic model of the radiatively inefficient accretion flow (RIAF) from [51]. (Taken from [52].)

directed to the observer is absorbed by the black hole. Figure 19 shows how the jet image varies as the inclination angle changes.

The image at large inclination angles has a characteristic double-sided shape, and contributions from jet and counter-jet radiation are approximately the same; at small angles, the image has the shape of a crescent, and its formation is governed by the counter-jet, and, if the inclination angle is zero, the image has a symmetric shape.

Apart from studying radiation intensity, of utmost importance is exploring its polarization. The polarization enables making some conclusions regarding both the magnetic field distribution and radiating environment properties. Figure 20 shows the rotation measure, and Fig. 21 the intensity distribution and a linear polarization map obtained in numerical models of the accretion flows and the jet in the vicinity of the central black hole in the galaxy M 87. We can see from Fig. 20 that the expected radiation rotation measures in the millimeter range are of the order of $10^4 - 10^7$, depending on the numerical model. Significant variations in the polarization vector direction near the black hole shadow should be noted in Fig. 19. This phenomenon is related to the Faraday rotation of the polarization plane of the jet-emitted radiation that passes through the accretion disk.

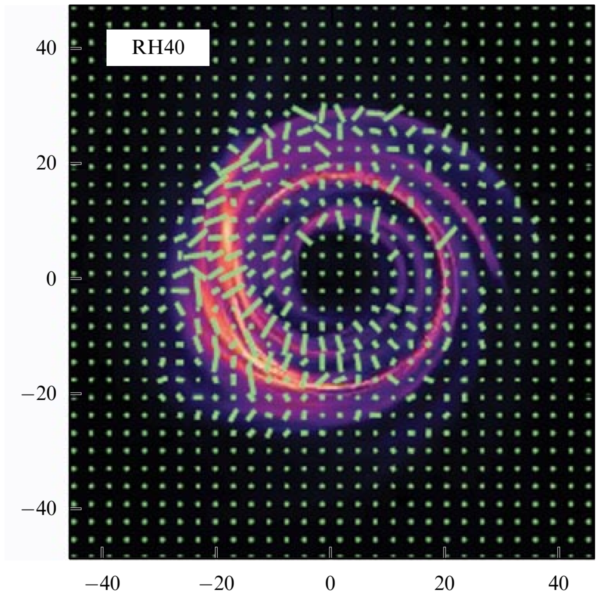

Figure 21. (Color online.) Image of the accretion disk and the jet calculated for the parameters that correspond to the black hole in the galaxy M 87 with a map of linear polarization superimposed on it. (Taken from [52].)

The shape and size of the accretion disk image can be used to make qualitative conclusions about physical characteristics of the environment surrounding the black hole. Figure 22 displays images of the vicinity of a black hole whose parameters correspond to those of the black hole in the Galaxy center as a function of the ratio of densities of nonthermal and thermal electrons in the accretion disk. It can be seen that as the fraction of nonthermal electrons increases, a characteristic 'halo' is formed around the black hole shadow.

We can see from the images of black hole surroundings in the millimeter range that some of them have the shape of a 'crescent'. This is only valid when the image is predominantly determined either by accretion disk radiation (the case of the black hole in the center of our Galaxy) or by radiation of the jet if the angle between the jet axis and the line of sight is not too large. This circumstance was used in [54, 55], where a simple analytic model was suggested for the intensity distribution and the corresponding visibility amplitude. The model consists of two circles with different radii. The outer circle center coincides with the direction to the source center located at the origin of angular coordinates on the celestial sphere, and the smaller circle is embedded into the larger one and shifted with respect to the reference point. It is assumed that only the region between the two circles radiates, and the intensity distribution in that region is assumed to be uniform. This distribution, together with the corresponding visibility amplitude, is shown in Figs 23 and 24. A two-dimensional Fourier image (in the angular coordinates of the model) has the form

$$C(u,v) = \frac{F}{\pi(R_{\rm out}^2 - R_{\rm in}^2)} \times \left[D(R_{\rm out},\rho) - D(R_{\rm in},\rho)\,\exp{(\mathrm{i}\delta)}\right], \qquad (7)$$

where F is the total flux, $D(R,\rho) = J_1(2\pi\rho)(R/\rho)$, $J_\nu(z)$ is the Bessel function, $\rho = (u^2+v^2)^{1/2}$ is the radial coordinate in the (u,v) plane, $R_{\rm out}$ and $R_{\rm in}$ are the outer and inner ring radii, $\delta = 2\pi\xi(R_{\rm out} - R_{\rm in})[\cos{(\phi u)} + \sin{(\phi v)}]$, the angle ϕ determines orientation of the internal ring with respect to the

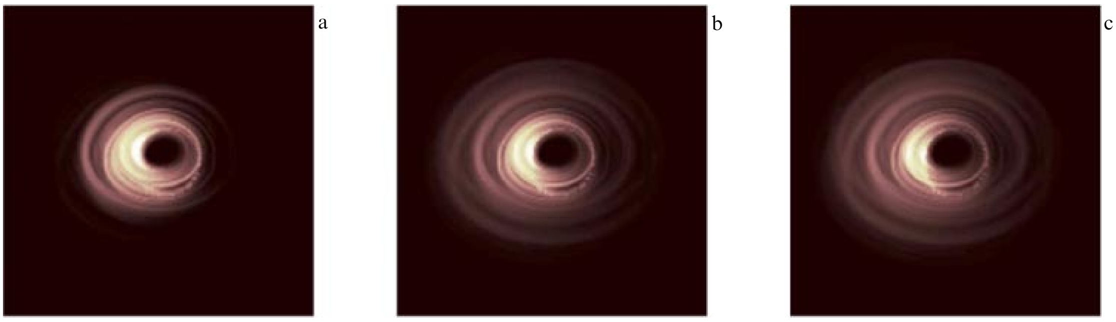

Figure 22. (Color online.) Image of an accretion disk surrounding a black hole, depending on the ratio of densities of thermal and nonthermal electrons: (a) $\eta = 0$, (b) $\eta = 0.02$, and (c) $\eta = 0.08$. (Taken from [53].)

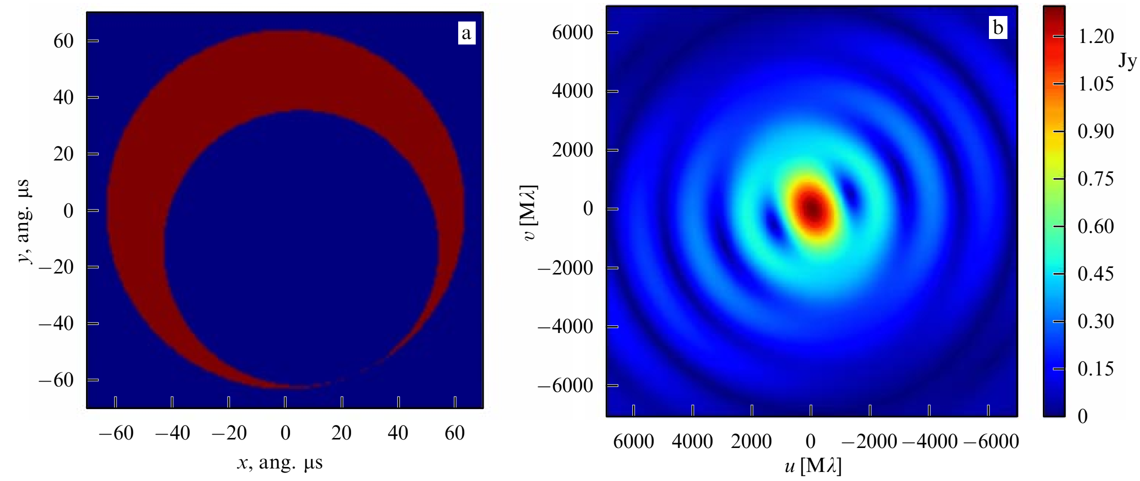

Figure 23. (a) Image of the black hole vicinity in an analytic 'crescent' model. (b) The corresponding visibility function. Parameters correspond to the black hole in the galaxy M 87. [Mλ] is the unit of measurement of the base projection onto the plane of spatial frequencies $u-v$ of a radio interferometer with a long baseline equal to $10^6\lambda$, where λ is the wavelength. (Taken from [54].)

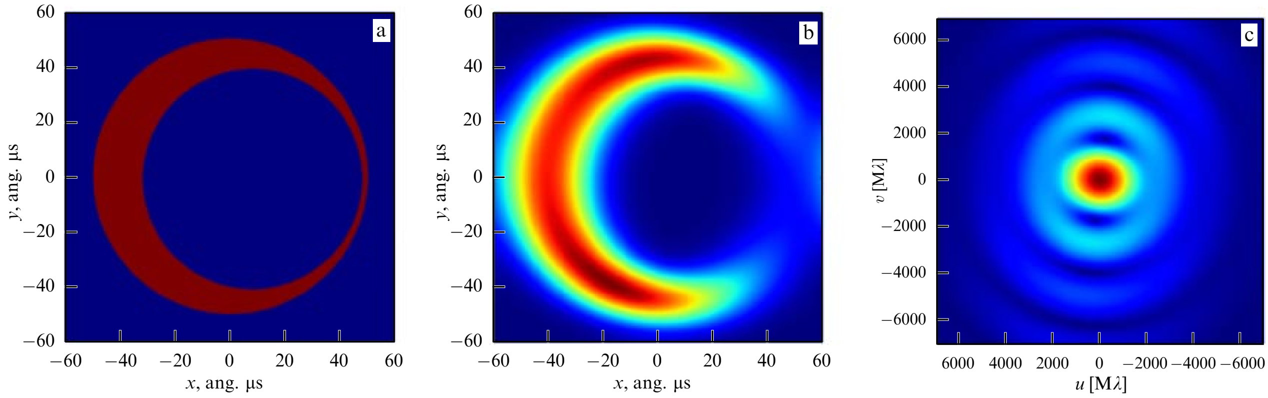

Figure 24. (a, c) Same as in Fig. 23 but with the parameters that correspond to the black hole in the center of our Galaxy. (c) Intensity distribution 'smeared' by scattering in the interstellar environment, a factor that proves to be of importance in the case of the Galaxy's center. (Taken from [55].)

angular coordinates, and the parameter ξ determines the 'shift' of the internal circle; the coordinates u and v are measured in units of the radiation wavelength λ. The best values of the model parameters are obtained by fitting the computation results. The following values have been found for the black hole in the center of M 87: $R_{\rm out} = 63.3$ ang. μs, $R_{\rm in}/R_{\rm out} \approx 0.78$, and $\xi \approx 1$ for a frequency of 230 GHz.

This model was used to search for candidates for observations by the planned space observatory Millimetron. Because the orientation of disks and jets in various objects of interest for observations is usually unknown, we used the visibility amplitude $\psi = \arcsin(v/\rho)$ averaged over the azimuthal angle in the $u-v$ plane:

$$F_{\rm av} = \sqrt{\frac{1}{2\pi}\int \mathrm{d}\psi\, C(u,v)\, C^*(u,v)} = \frac{F}{\pi(\rho R)(1-r^2)}$$

$$\times\sqrt{J_1^2(x_1)+J_1^2(x_2)\,r^2 - 2J_1(x_1)\,J_1(x_2)\,J_0(x_3)\,r}\,, \quad (8)$$

where $R \equiv R_{\rm out}$, $r = R_{\rm in}/R_{\rm out}$, $x_1 = 2\pi R\rho$, $x_2 = 2\pi r R\rho$, and $x_3 = 2\pi(1-r)\,R\rho$. The parameter R was set to be directly proportional to the black hole mass and inversely proportional to the distance to the black hole:

$$R = 8.3 \times 10^{-10}\,\frac{M_9}{D_1}\;[\text{rad}]\,, \tag{9}$$

where M_9 is the black hole mass measured in units of $10^9 M_\odot$, and D_1 is the distance to the black hole in megaparsecs. For the mass of the black hole in the galaxy M 87 that is set equal to $6.6 \times 10^9 M_\odot$ and the distance $D = 17.9$ Mpc, Eqn (9) yields the value $R \approx 6.3$ ang. µs, which coincides with the value quoted above.

3. Catalog of objects that can be observed with the Event Horizon Telescope and the Millimetron space laboratory

3.1 Criteria for selecting objects for radio interferometric observation with a super-long baseline using the Millimetron and the Event Horizon Telescope

As a preliminary selection of extragalactic sources suitable for observations by the Millimetron observatory, we used the NASA/IPAC Extragalactic Database [4] and publications containing SMBH catalogs [56–59] to compile an initial list of galaxies (see [60]) that meet the criteria of availability of observational data on: 1) the presence of SMBHs in their centers and 2) the intensity of radiation from compact sources in galaxy centers in the frequency range 10–1000 GHz. It was assumed that this radiation is related to the activity of central black holes.

Next, a secondary list of objects was created using the following criteria. Three 'basic' frequencies (84, 211, and 240 GHz) were introduced. The sources were selected from the initial list for which data on the frequencies at which radiation fluxes were measured differ from any of the basic frequencies by no more than 50 GHz; the fluxes at those frequencies were assumed to be approximately equal to those at reference frequencies.

If data for more than one observation at various frequencies were available within the selected range, the radiation flux for each reference frequency was adopted to be approximately equal to its value at the nearest frequency for which such data were available. The flux values selected in this way were used in Eqn (8) and the ρ values accessible for the Millimetron were calculated using the data on possible minimum and maximum observational baselines for the selected orbit of the spacecraft and given coordinates of specified sources. We then checked for each basic frequency whether there is an observational baseline range where the value of the averaged flux $F_{\rm av}$ determined using (8) is larger than the detection thresholds found using the Millimetron response curve. The limit values of the fluxes were taken to be 0.483 mJy for the basic frequency of 84 GHz, 2.94 mJy for 211 GHz, and 6.45 mJy for 240 GHz. We note that $F_{\rm av}$ oscillates at large ρ, and therefore to determine the minimum and maximum observation baselines for which $F_{\rm av}$ exceeds the threshold value, either we used the smallest and largest available baseline values where the flux $F_{\rm av}$ was equal to the threshold value, or, if the averaged flux at the minimum baseline available for the Millimetron exceeded the threshold value, the minimum observation baseline was set equal to the base accessible for the Millimetron. Examples of the $F_{\rm av}$ dependence on the observation baseline (measured in units of Earth's diameter $D_{\rm Earth}$) for two specific sources are shown in Figs 25 and 26.

The criterion for being included into the list of candidates for observations with the Millimetron is the availability of a baseline range for which $F_{\rm av}$ exceeds the detection threshold for at least one of the basic frequencies. We note that this criterion is apparently model dependent, because it assumes that all objects suitable for observations have images similar to that of the black hole in the galaxy M 87; it can only be used for a preliminary selection of candidates in a situation where many of their properties are unknown.

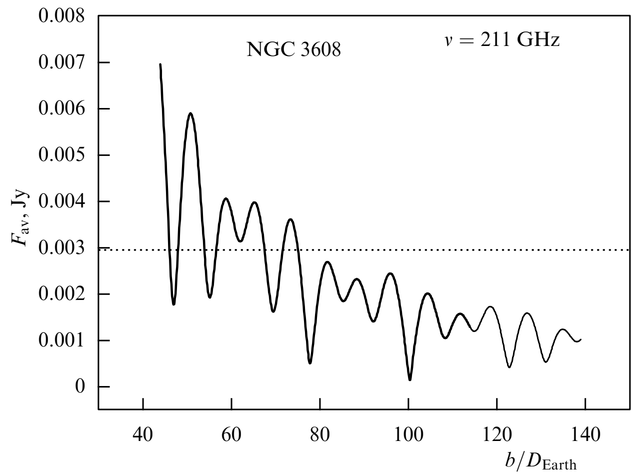

Figure 25. Example of how the averaged flux $F_{\rm av}$ (solid curve) depends on the projection of the interferometer base onto the plane perpendicular to the line of sight (below, the interferometer observational base), $b = \lambda\rho$ for the galaxy NGC 3608 and the observation frequency 211 GHz. Displayed are only the baseline values that are accessible to the Millimetron. The horizontal dotted line shows the sensitivity limit at the given frequency. The minimum and maximum observational bases between which observations are possible in principle were taken to be equal to the minimum and maximum of b at which the solid and dotted lines cross. $D_{\rm Earth}$ is Earth's mean diameter.

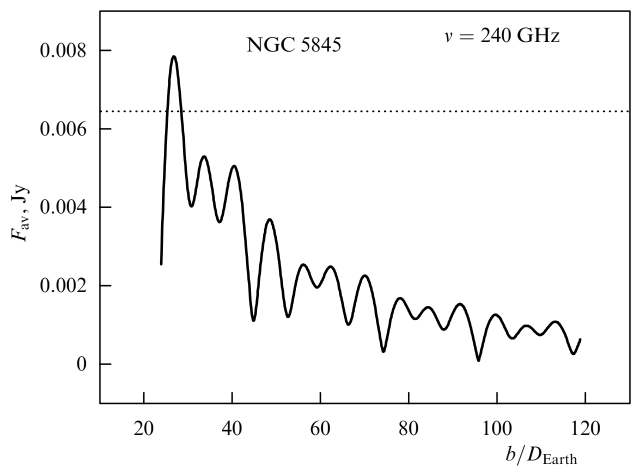

Figure 26. The same as in Fig. 25 but for the galaxy NGC 5845 and the observation frequency of 240 GHz.

[4] See https://ned.ipac.caltech.edu/; NASA — National Aeronautics and Space Administration; IPAC — Infrared Processing and Analysis Center.

In the future, we plan to consider more elaborated theoretical models of the selected candidates and develop a more realistic assessment of their detectability by the Millimetron. The main features of the selected objects are displayed in Table 5 (see Section 3.3): the SMBH mass, the distance to the object, the angular dimensions defined as the ratio of the gravitational radius $r_g = GM/c^2$ to the distance to the source D, and coordinates on the celestial sphere. For the same sources, Table 6 presented in Section 3.3 displays the fluxes at basic frequencies, the range of observational baseline projections accessible to the Millimetron, the baseline range within which observations are possible according to the sensitivity criterion described above at three basis frequencies and the corresponding flows on the minimum and maximum baselines, and the ratio η of bolometric and Eddington luminosities.

We used the complete list of sources for which VLBI observations by the Millimetron are possible according to the adopted criterion to create a list of the 'best' candidates for which the criterion is fulfilled at all three basic frequencies. The SMBH in the galaxy M 87 was added to the list, although the criterion is only fulfilled for it at the frequency of 84 GHz, because this black hole — along with the one in the Galaxy center — is an object that is the most studied using both theoretical and observational methods. The list includes 20 sources: Sgr A*, M 87, IC 1459, NGC 5128, IC 4296, OJ 287, NGC 5845, NGC 5077, NGC 3585, Cygnus A (3C 405), M 82 (NGC 3034), Fornax A (NGC 1316), NGC 821, NGC 6251, PKS 2126-158, Perseus A (NGC 1275), 3C 120, Her A (3C 348), 3C 273, and NGC 1068 (M 77). Sections 3.2 and 3.3 contain additional information on these sources, pertaining to both the black holes themselves and the main properties of the host galaxies.

We note that the list above contains the quasar OJ 287 that exhibits a light curve variation with an 11-year period. OJ 287 is considered to be the most plausible candidate for a binary black hole, its more massive component probably having a mass of the order of 20 billion solar masses and thus potentially being one of the most massive black holes ever discovered. VLBI observations of that system will allow confidently confirming or rejecting the hypothesis that it contains a binary black hole.

3.2 Basic properties of the two most studied accreting black holes located in the centers of the Milky Way and M 87 galaxies

Among the accreting black holes, those located in the Galaxy center (the Sgr A* source) and the center of the galaxy M 87 stand out as the most studied in the entire range of frequencies in observations made by both individual telescopes and VLBI methods. They are also the main candidates for observation with the EHT. Due to this circumstance, it is essentially the parameters of these sources alone that were used in theoretical and experimental models for the images of black hole vicinities (see Section 2.5). Because these objects are of special importance, we present a detailed review of their main properties in Sections 3.2.1 and 3.2.2.

3.2.1 Sagittarius A*. Located in the center of the Milky Way galaxy at a distance of $\simeq 8.3 \pm 0.4$ kpc from the Sun, Sgr A* is a compact source of radiation in a broad range from radio waves to X-rays. Sgr A* is the SMBH closest to us, with $M \approx 4.3 \pm 0.5 \times 10^6 M_\odot$ and $R_g = 2GM/c^2 \approx 1.27 \times 10^{12}$ cm [61, 62]. The Schwarzschild radius is observed at a distance of ~ 8 kpc and has the angular size 10 ang. μs, which is the largest among those known. Interferometric observations in the millimeter (submillimeter) range are an ideal tool to study this object. Multifrequency monitoring indicates that the nucleus activity that occurs on a scale of several R_g is exhibited in the form of short-term variability and bursts in all radiation bands.

Interferometric observations were performed in the millimeter spectrum range as part of the initial stage of the EHT project in April 2009 (days 95 to 97) [63]. Sgr A* and several gauge sources were observed by four telescopes from three observatories: James Clerk Maxwell Telescope (short name J), Arizona Radio Observatory's Submillimeter Telescope (S), and two telescopes of the Combined Array for Research in Millimeter-wave Astronomy (C and D) (see [63]). The observations were conducted at the wavelength $\lambda = 1.3$ mm ($\nu \approx 231$ GHz). The estimated brightness temperature of the source for that wavelength is 2×10^{10} K [64].

Figure 27 shows observation results for each day (95, 96, and 97). Figure 27a displays the correlated flux density as a function of time, and Fig. 27b displays the same values but with corrections made (see [63]). A specific feature of Sgr A* is its time variability. A constant (within the level of errors) flux density was observed on days 95 and 96, while on day 97 it increased by 17%. The observation data were used to fit two models of the source intensity distribution: one with a Gaussian intensity distribution, and the other with a ring-shaped distribution. The flux density for the Gaussian model proved to be 2 Jy, and the angular size was 41 ang. μs.

The density of the flux from the Sgr A* source as a function of frequency is shown in Fig. 28. The Sgr A* radio spectrum is shown in Fig. 29. The average spectral index is $\alpha = 0.5$ for the frequency range 22–236 GHz [66] and $\alpha = 0.47$ for 8.4–340 GHz [68]. It is believed that the radio waveband is determined by radiation of synchrotron photons and their self-absorption. A transition from an optically thick spectrum to an optically thin one occurs at a wavelength of the order of 1 mm [61]. X-ray radiation is interpreted as generated due to Compton scattering of synchrotron photons.

Important information about the properties of Sgr A* comes from studying its linear polarization. The visible absence of linear polarization at wavelengths longer than some specific value and a rapid increase in the polarization degree at shorter wavelengths can yield an upper bound on the rotation measure (RM) and the accretion rate ($\dot{M}$) at distances of 10–1000R_g [69]. An explanation is that a distributed and/or sufficiently dense accretion flow can depolarize radiation. Linear polarization was detected for the first time in [70] at frequencies over 100 GHz (wavelengths less than 3 mm) after unsuccessful searches at lower frequencies. The Sgr A* polarization at millimeter and submillimeter wavelengths is known to vary in both magnitude and polarization angle position on a time scale of several hours. Observations at two frequencies, 82.76 and 86.31 GHz ($\lambda \approx 3.5$ mm), have been made for five epochs [69]. The average flux density for a frequency of 82.76 GHz turned out to be 1.93 ± 0.07 Jy, and the flux variation amplitude for all five epochs was 0.18 Jy. Polarization could be measured for each epoch. Figure 30 shows the average polarization degree as a function of frequency. The polarization degree increases as the frequency increases.

Averaged polarization data were combined in [69] to determine, under the assumption of equal distribution among magnetic, kinetic, and rotational energies, the rota-

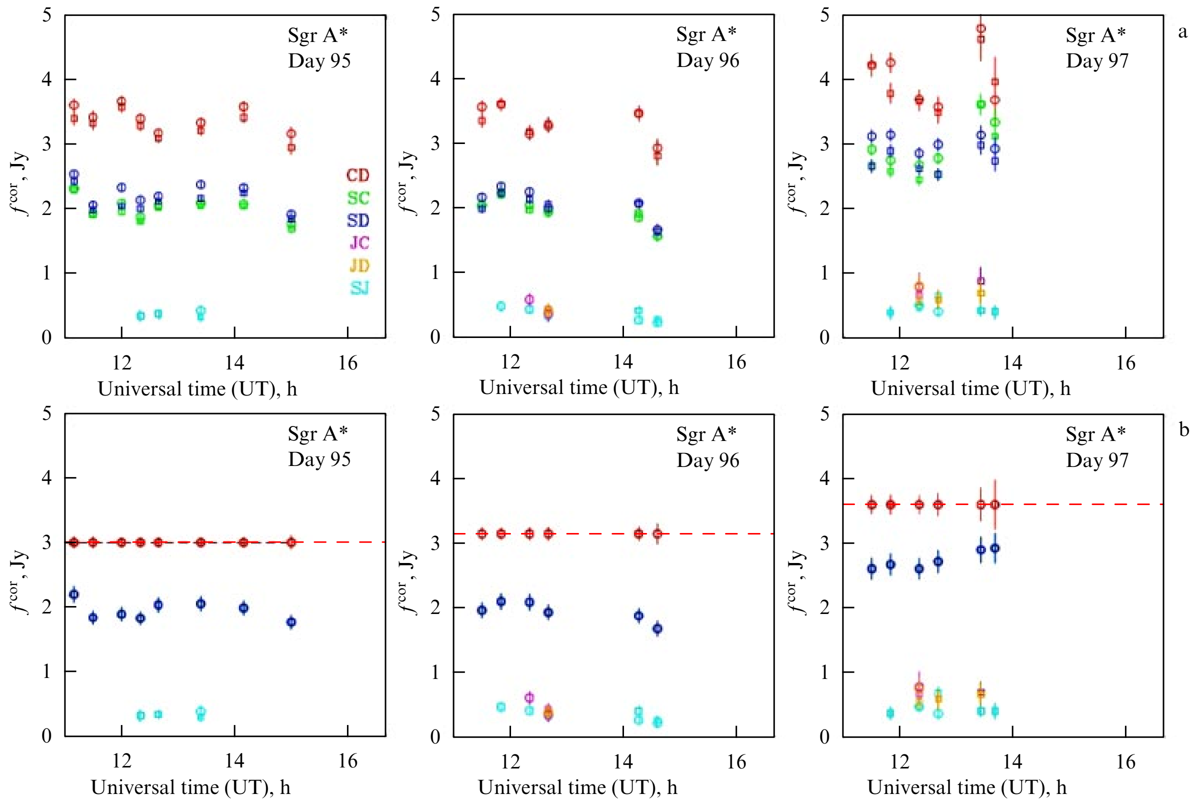

Figure 27. (Color online.) Correlated flux density obtained in observing Sgr A* in 2009: (a) without introducing corrections and (b) with the corrections made. Latin characters (CD, SC, etc.) denote the pair of telescopes that participated in the observations.

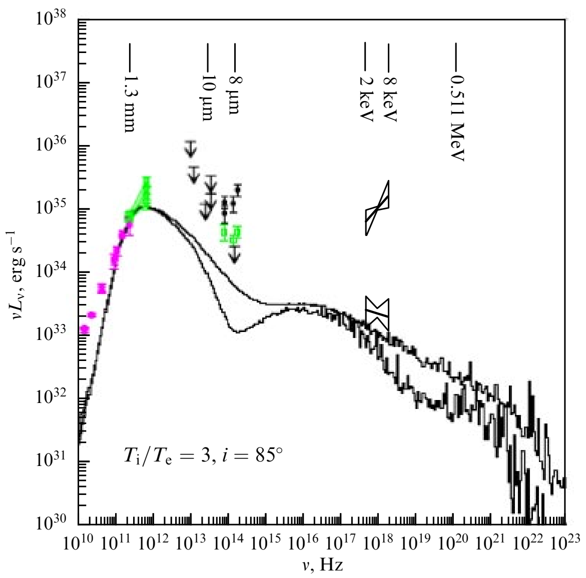

Figure 28. (Color online.) Radiation flux from the Sgr A* source as a function of frequency. Symbols of different colors show observations and upper constraints obtained at various moments of time. Black curves show results of simulations using a model of a radiatively inefficient accretion disk. (Taken from [65].)

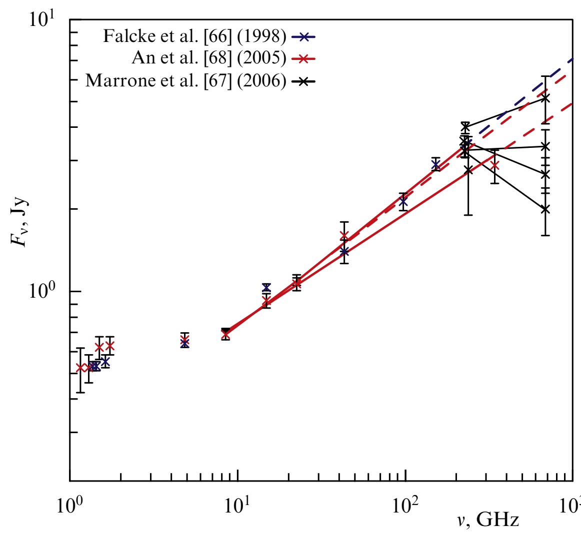

Figure 29. (Color online.) Radio spectrum of the Sgr A* source.

tion measure $\mathrm{RM} = (-4.4 \pm 0.3) \times 10^5$ rad m^{-2} and the estimated accretion rate $\dot{M} \approx (0.2-4) \times 10^{-8} M_\odot$ year^{-1}. Observations at larger frequencies, 227 and 343 GHz (≈ 1 mm), were performed in June and July 2005 [71]. The average rotation measure obtained in [70] is $\mathrm{RM} = -5.6 \pm 0.7 \times 10^5$ rad m^{-2}. Polarization measurements in the frequency range 230–345 GHz are reported in [72]. These data are shown to vary on a few-hour scale. Although the variability may be due to both internal and external processes, the variability on a few-hour scale is an indication that these processes occur in a region very close to the black hole, thus confirming the importance of multifrequency measurements for exploring Sgr A*.

3.2.2 M 87. The distance to the galaxy M 87, a dominating elliptic galaxy in a galaxy cluster located in the Virgo cluster, is 16.7 Mpc (see [73]). The mass of the SMBH located in the

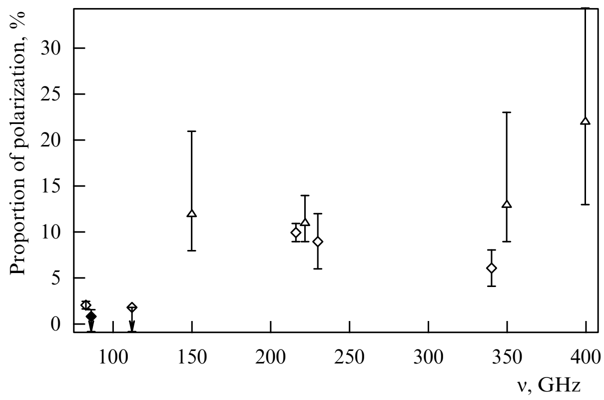

Figure 30. Average degree of polarization as a function of frequency.

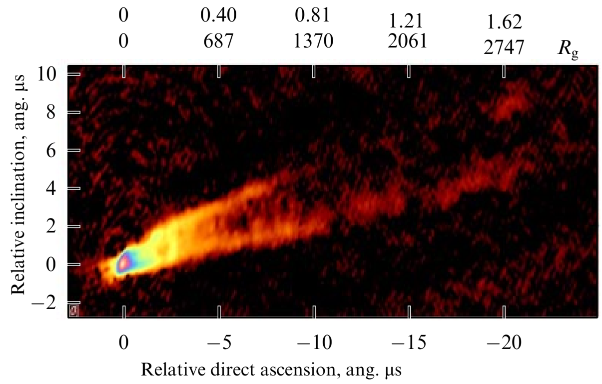

Figure 31. Image of M 87 obtained by VLBA at a frequency of 43 GHz on 12.01.2013.

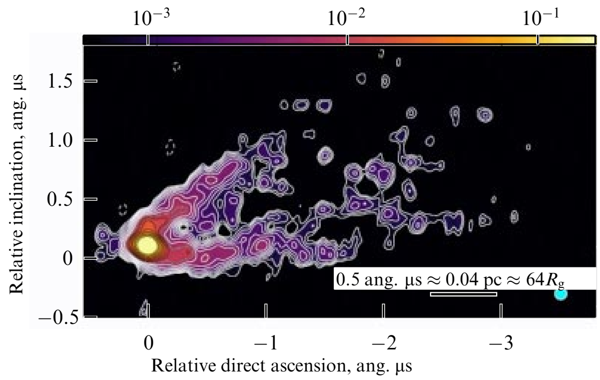

Figure 32. Image of the M 87 jet obtained at a wavelength of 3 mm.

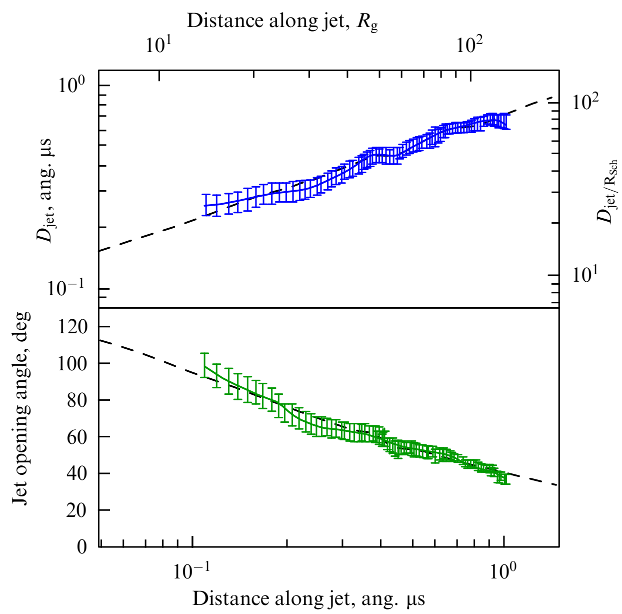

Figure 33. Internal profile of the M 87 jet.

M 87 center is $M = 3.5^{+0.9}_{-0.7} \times 10^9 M_\odot$ according to a gasdynamic estimate (see [74]) and $M = 6.6 \pm 0.4 \times 10^9 M_\odot$ according to stellar-dynamics arguments [75]. The Schwarzschild radius for the latter estimate is $R_g = 1.95 \times 10^{10}$ km ($R_g = 130$ a.u.), corresponding to a size of 8 ang. μs, the largest angular size of a black hole that has a radio jet with a well-studied structure [73]. Thus, M 87 is the best candidate for observing the jet base where it is accelerated and collimated.

The M 87 jet has a wide opening angle near the base and shows brightening to the edge, as follows from observations by the Very Long Baseline Array (VLBA) at a frequency of 43 GHz (≈ 7 mm) [76]. As was shown for all sufficiently high frequencies of VLBI observations of M 87*, the structure of brightening to the edge is parabolically shaped and is approximately described by the formula $r \sim z^{0.58}$. This parabolic shape continuously, extends to a structure (knot in the jet HST1) located at a distance of 65 pc from the center, after which the jet shape changes to conic. A counter-jet is also observed. Its existence had been suggested by many authors (see, for example, a discussion of VLBI observations at 43 GHz in [77]) and was substantiated in [78], where data of the VLBI observations at 15 GHz were used. The apparent propagation velocity in the jet is subluminal on small scales [78]. The acceleration region is located on a scale of a fraction of an angular second. A high superluminal velocity, about $6c$, is observed near the HST1 knot in the optical band (see [79]) and radio band (see [80]).

Figure 31 shows images of the M 87 nucleus and jet (1 ang. μs = 0.08 pc). Figure 32 shows the jet displayed with high resolution at $\lambda = 3$ mm. The intensity peak is 522 mJy per beam. Figure 33 presents the collimating profile that corresponds to $r \sim z^{0.523}$.

The rotation measure determined at centimeter wavelengths is several hundred rad m^{-2} for the jet on scales of several kpc [81, 82]. In [80], regions were found where the rotation measures have opposite signs. The rotation measures in the M 87 nucleus in the millimeter range (230 GHz) were obtained for the first time in [84]. The estimated rotation measure of the nucleus is $|\mathrm{RM}| < 7.5 \times 10^5$ rad m^{-2} (see [84]), yielding the estimated mass flow $\dot{M} < 9.2 \times 10^{-4} M_\odot$ per year at a distance of $21 R_g$ from the black hole. This value is two orders of magnitude smaller than the estimated mass flow on the Bondi radius [84], indicating the possible occurrence of strong outflows in the accretion disk. We note that the rotation measure can be obtained in the millimeter band more reliably than in other bands because depolarization and absorption effects are less significant in that band.

Figures 34 and 35 show data on the radiation flux from the M 87 center as a function of frequency and a comparison of those data with the shapes of the spectra of other active galaxies, type I and II Seyfert galaxies, and radio-loud quasars. Many features are missing in the spectrum of the

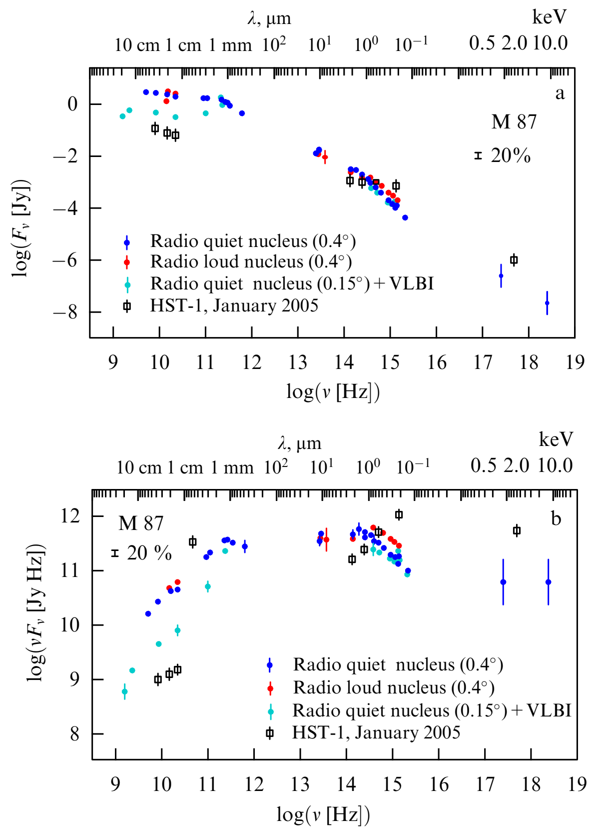

Figure 34. (Color online.) (a) Radiation flux density and (b) radiation flux coming from the vicinity of the M 87 center limited by a radius of 0.4 ang. s (32 pc) as a function of frequency. Symbols of different colors show observations performed in various epochs: blue and red symbols correspond to the epochs of quiet and active states of the nucleus and light-blue symbols show combined data obtained with the maximum resolution, 0.15 ang. s (12 pc), using VLBI methods. Squares show observations of the HST-1 knot. (Taken from [29].)

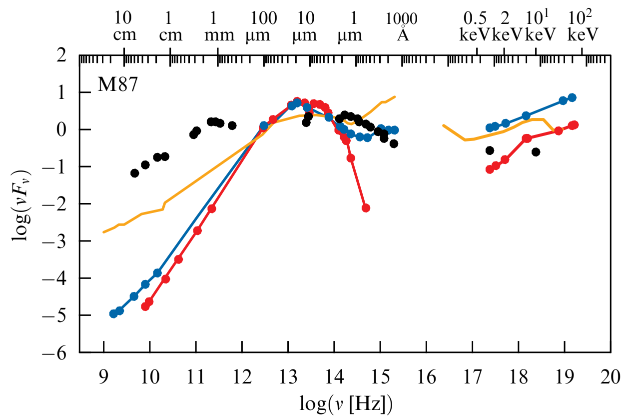

Figure 35. (Color online.) Radiation flux from the M 87 center in a quiet state as a function of frequency (black dots) in comparison with data on type-I Seyfert galaxies (blue symbols), type II (red symbols), and radio-loud quasars (yellow curve). All fluxes are normalized to the same mean value. (Taken from [29].)

M 87 center that are typical of active galactic nuclei: an ultraviolet and/or infrared power excess that is indicative of the presence of an accretion disk and/or dust torus. The M 87* spectrum can be fully explained in some theoretical models by jet radiation, while the contribution from accretion disk radiation is not obvious.

3.3 Description of the sources

The 'best' sources have been selected by applying the criterion formulated in Section 3.1 (our initial work catalog contained 219 sources). Because the properties of the vicinities of the black holes in the center of the Galaxy and M 87 are described in Section 3.2, they are not included into that list. A brief description of the sources is presented below.

IC 1459. The host galaxy is an E 3-4 type. The radio source has a flat spectrum. The SMBH mass was determined using methods of stellar dynamics.

NGC 5128 (Cen A). The host galaxy, which is an S0 type, is one of the closest and brightest galaxies in the sky. Being a strong radio source, it is classified as a type II Seyfert galaxy. The SMBH mass was determined using methods of stellar dynamics.

IC 4296. The host galaxy is elliptic and belongs to a group. The radio source features a flat spectrum and has a jet.

OJ 287. The object has been observed for more than 100 years (in the optical range) and exhibits variability with a period of about 12 years, which is interpreted as activity of a binary SMBH. Classified as a BL Lac-type object, it features a flat spectrum and rather high optical polarization (> 3%). It has a jet or an extended structure.

NGC 5845. The host galaxy is elliptic. The SMBH mass was determined using methods of stellar dynamics.

NGC 5077. The host galaxy is an E 3-4 type and is a member of a pair. Classified as a Seyfert galaxy, LINER 1.9, it has a flat radio spectrum. The central radio source has not been resolved. The SMBH mass was determined using methods of gas dynamics.

NGC 3585. The SMBH's host galaxy, a member of a loose group, is, according to various estimates, a type E6 or E/S0. Jet is not seen. The SMBH mass was determined using methods of stellar dynamics.

Cyg A (3C 405). This galaxy seems to be a spiral one. The radio source has a jet. It belongs to the morphological type FR II.

M 82 (NGC 3034). This is a spiral galaxy that experiences a star formation burst. Belonging to a pair with M 81, it is observed from the edge (80°). The galaxy belongs to the morphological type FR I. The SMBH mass was determined using methods of stellar dynamics.

NGC 1316 (Fornax A). The galaxy, which is a product of a merger that occurred about 3 bn years ago, is a member of a pair. Depending on the data, it can be classified as an SAB or S0 type. The radio source associated with the galaxy center has a radio jet. It belongs to a set of active galactic nuclei (AGNs) with low X-ray luminosity. The SMBH mass was determined using methods of stellar dynamics.

NGC 821. It is an isolated galaxy of the E6 type [86]. According to other data [87], it is a galaxy viewed almost edge-on with a rapidly rotating disk-like component. The galaxy is a flat-spectrum radio source. The SMBH mass was determined using methods of stellar dynamics.

NGC 6251. The SMBH's galaxy is elliptic. Being a member of a pair, it belongs to the morphological type FR I. The SMBH mass was determined using methods of stellar dynamics.

PKS 2126-158. This is a flat-spectrum radio source. VLBI observations indicate that it has a nucleus and a jet [88].

NGC 1275 (Perseus A, 3C 84). This is the central galaxy of a galaxy cluster in Perseus (A 426). The galaxy exhibits evident features of an earlier merger and belongs to peculiar galaxies. The NGC-related radio source, which has a flat spectrum, is classified as an LIRG (Luminous InfraRed

Galaxy) and as Seyfert I, LINER. It has ‘radio ears’ and a jet. The SMBH is determined using data on the distribution of molecular hydrogen velocities [89].

3C 120. The host galaxy is assumed to be a type S0. It is a flat-spectrum radio source. The AGN is classified as Seyfert I. There is a radio jet. The SMBH mass is measured using the reverberation method [90, 91].

Her A (3C 348). This is a supermassive galaxy whose estimated mass is $10^{15} M_{\odot}$. The host galaxy is a cluster cD galaxy, E 3-4. The source has an extremely long radio jet. The galaxy is a morphological type FR I or FR I/II.

3C 273. This is the brightest quasar in the sky. The flat-spectrum radio source, which belongs to the class ULIRG (Ultra Luminous InfraRed Galaxy), has a radio jet. The SMBH mass is estimated using the reverberation method [90]. VLBI observations were performed in 2012–2014 by the RadioAstron ground–space observatory [92].

NGC 1068 (M 77). This is one of the most studied galaxies with an AGN [93]. It has a bar that ends with two spiral branches. The bar, whose angular scale is 120″, is oriented along the minor axis and has a tilt of 40°. The bar is classified as Seyfert II, LIRG, and has a compact radio jet. The SMBH mass was determined using maser data.

Table 5 shows the main characteristics of the sources listed above. The first column contains the object name that is used most often. For convenience, the object’s second

Table 5. Main characteristics of the SMBHs accessible for observations by the Millimetron observatory.

Object	$M/(10^8 M_{\odot})$	D_a, Mpc	Angular size, μs	Right ascension, h min s	Declination, degree min s	Reference
Sgr A*	0.041 0.0431	0.008 0.00833	5.06 5.11	17 45 40.02	−29 00 28.17	[56, 57] [58, 59]
NGC 4486 (M 87)	36 63 62	17 17 16.7	2.09 3.66 3.67	12 30 49.42	12 23 28.0	[56] [57] [58, 59]
IC 1459	28 25	30.9 28.9	0.89 0.85	22 57 10.61	−36 27 44.0	[56, 57] [58, 59]
NGC 5128 (Cen A)	3 0.7 0.57	4.4 4.4 3.62	0.67 0.16 0.16	13 25 27.61	−43 10 08.8	[56, 57] [56, 57] [58, 59]
IC 4296	13.0	49.2	0.26	13 36 39.053	−33 57 57.3	[58, 59]
OJ 287	180	930	0.19	08 54 48.88	20 06 39.6	[94]
NGC 5845	2.9 5.4 4.9	28.7 28.7 25.87	0.10 0.19 0.19	15 06 00.8	01 38 01.8	[56] [57] [58, 59]
NGC 5077	8.0 8.6	44.9 38.7	0.18 0.22	13 19 31.670	−12 39 25.08	[56, 57] [58, 59]
NGC 3585	3.4 3.3	21.2 20.5	0.16 0.16	11 13 17.1	−26 45 17	[56, 57] [58, 59]
Cygnus A (3C 405)	25 27	224 257	0.11 0.10	19 59 28.4	40 44 02.1	[95] [56, 59]
NGC 3034 (M 82)	0.3	3.2 – 5.5	0.09 – 0.05	09 55 52.7	69 40 46	[96]
NGC 1316 (Fornax A)	1.5	18.6	0.08	03 22 41.8	−37 12 29.52	[57 – 59]
NGC 821	0.42 1.8 1.6	25.5 25.5 23.4	0.02 0.07 0.07	02 08 21.15	10 59 41.53	[56] [57] [58, 59]
NGC 6251	6 6.1	106 108	0.06 0.06	16 32 32.0	82 32 16	[56, 57] [58, 59]
PKS 2126-158	100	1546	0.06	21 29 12.2	−15 38 41	[97]
NGC 1275 (Perseus A)	3.4	75	0.04	03 19 48.1	41 30 42	[59, 89]
3C 120	0.2 0.5 0.54	136 141	0.001 0.004 0.004	04 33 1.1	05 21 16	[90] [91] [59]
Her A (3C 348)	1.1 20	643 643	0.002 0.03	16 51 08.15	04 59 33.32	[98] [95]
3C 273	5.5	563	0.01	12 29 06.6997	02 32 08.598	[90]
NGC 1068 (M 77)	0.086 0.084	15.4 15.9	0.006 0.005	02 42 40.7	−00 00 48	[56, 57] [58, 59]

name is quoted for some sources (in parentheses). The second column contains the mass of the central black hole of the corresponding galaxy in units of $10^8 M_\odot$. Different values correspond to different measurements, information about which can be found using the references displayed in the corresponding line of the last column. As was correctly indicated in [85], the estimated SMBH masses obtained using various methods can differ for some objects by a factor of 10 (see Table 1 in [85]). The methods based on gas or stellar dynamics are considered to be more reliable than reverberation or statistical methods (a brief review of the methods can be found in the same publication [85] or the references therein). Therefore, it is only the first digit that is valid in the quoted mass values.

The third column contains the distance to the source (galaxy) expressed in megaparsecs. We took the distances either from the references quoted in the table or from the Internet resource http://ned.ipac.caltech.edu; otherwise, they were calculated using the red shift as an angular distance, assuming the dimensionless dark energy density $\Omega_\Lambda = 0.7$, the dark matter density $\Omega_m = 0.3$, and the Hubble constant $H_0 = 70$ km s^{-1} Mpc^{-1}. Because distances to almost all sources are no longer than 100 Mpc, the model effect was insignificant and was of importance only for such distant monsters as OJ 287 and PKS 2126-158.

The fourth column contains SMBH's angular scales. The angular size of the source is one of the most important characteristics that determines whether the object can be reliably observed. To reflect the importance of that parameter, the sources are arranged in Table 5 in decreasing order of these values. The angular scale here means the angular size of the black hole's gravitation radius, $\theta = GM/(c^2 D_a)$, equal to half the Schwarzschild radius (D_a is the angular distance). Expressed in arc microseconds, it coincides (within 1.2%) with the ratio of the SMBH mass, measured in $10^8 M_\odot$ units, and the distance in Mpc, an estimate that is very convenient for rapid assessment of the angular scale of the black hole 'image'. [5]

The fifth and sixth columns contain source coordinates, right ascension and declination, as of the epoch J2000.

The selected sources are listed in Table 6 in the same order as in Table 5. It displays the base frequency (second column), the observed dispersion of values, and the value or an estimate

[5] We recall that the angular diameter of a black hole is significantly larger, by a factor of 10, than the angular scale.

Table 6. SMBHs accessible for observations by the Millimetron observatory: flows.

Object	Frequency, GHz	Flux, Jy	Base projection range/$D_{\rm Earth}$	$D^{\min}/D_{\rm Earth}$	Flux, Jy 84 GHz 211 GHz 240 GHz	$D^{\max}/D_{\rm Earth}$	Flux, Jy 84 GHz 211 GHz 240 GHz	η
1	2	3	4	5	6	7	8	9
Sgr A*	43 100 240	1.3 – 1.9 2.1 – 2.4 2.8 – 4.1	7 – 98	7.0 7.0 7.0	0.031 0.010 0.018	97.8 28.1 14.2	0.0006 0.0030 0.0066	10^{-9}
NGC 4486 (M 87)	43 100 240	13 0.5 – 2.4 1	47 – 139	84: 47.0	0.01	138.9	0.0006	2×10^{-5} (n)
IC 1459	43 100 240	~0.4 0.26 ~0.5	2 – 141	2.0 2.0 2.0	0.19 0.16 0.17	140.9 38.9 19.3	0.0009 0.003 0.007	4×10^{-3}
NGC 5128 (Cen A)	43 100 240	32 – 72 41 6	8 – 136	8.0 8.0 8.0	35.3 2.29 1.91	135.9 135.9 135.9	2.01 0.075 0.064	0.3 (n)
IC 4296	43 100 240	0.7 – 1.2 0.7 ~0.6	2 – 130	2.0 2.0 2.0	0.68 0.40 0.37	129.9 115.6 57.3	0.003 0.003 0.007	3×10^{-6}
OJ 287	43 100 240	1.6 – 2.9 4.5 1.4 – 3	18 – 122	18.0 18.0 18.0	1.8 0.46 0.37	121.9 121.7 121.9	0.18 0.003 0.02	5×10^{-3}
NGC 5845	43 100 240	~ 0.003 ~0.01 ~0.02	24 – 119	24.0 24.0 24.0	0.03 0.02 0.007	118.9 104.9 49.9	0.005 0.003 0.006	4×10^{-6}
NGC 5077	43 100 240	~0.3 0.66 0.4	17 – 129	17.0 17.0 17.0	0.27 0.06 0.05	128.9 128.9 83.2	0.023 0.004 0.007	5×10^{-7}
NGC 3585	43 100 240	~0.002 ~0.005 ~0.01	0 – 141	0.1 0.1 0.1	0.005 0.01 0.01	71.1 15.6 4.6	0.0005 0.003 0.006	6×10^{-8}
Cygnus A (3C 405)	43 100 240	~1.3 ~1 0.5	86 – 125	86.0 86.0 86.0	0.30 0.13 0.10	125.0 125.0 125.0	0.33 0.060 0.039	3×10^{-3}

Table 6 (continued)

1	2	3	4	5	6	7	8	9
NGC 3034 (M 82)	43 100 240	0.7 – 1.3 0.8 – 1 0.7	70 – 114	70.0 70.0 70.0	0.27 0.028 0.034	11.4 11.4 11.4	0.14 0.022 0.017	4×10^{-5}
NGC 1316 (Fornax A)	43 100 240	3 – 11 0.7 – 1.4 2.5	37 – 138.9	37.0 37.0 37.0	0.6 0.4 0.3	138.9 138.9 138.9	0.16 0.03 0.05	7×10^{-8} (n)
NGC 821	43 100 240	~ 0.07 0.086 ~ 0.05	12 – 121	12.0 12.0 12.0	0.08 0.03 0.03	120.9 87.6 54.3	0.01 0.003 0.006	5×10^{-8}
NGC 6251	43 100 240	1 – 1.5 0.9 ~ 0.8	82 – 122	82.0 82.0 82.0	0.28 0.062 0.036	122.0 122.0 122.0	0.21 0.038 0.030	5×10^{-7} (n)
PKS 2126-158	43 100 240	0.5 0.5 0.08	21 – 136	21.0 21.0 21.0	0.25 0.027 0.024	135.9 135.9 62.8	0.038 0.004 0.007	1
NGC 1275 (Perseus A)	43 100 240	6.9 – 7.9 7.7 4.8 – 27	20 – 98.9	20.0 20.0 20.0	7 16 14	98.9 98.9 98.9	2 2.9 0.52	2×10^{-4} (n)
3C 120	43 100 240	1.9 – 2.5 2.1 – 3 1.6	9 – 108	9.0 9.0 9.0	3 1.6 1.6	107.9 107.9 107.9	3 1.5 1.4	0.02
Her A (3C 348)	43 100 240	~ 0.2 0.2 ~ 0.2	1 – 98	1.0 1.0 1.0	0.2 0.2 0.1	97.9 97.9 97.9	0.06 0.01 0.01	4×10^{-4}
3C 273	43 100 240	8 9 – 12 6 – 11	36 – 141	36.0 36.0 36.0	25 9 8.5	140.9 140.9 140.9	16 3.6 3.1	$\lesssim 8$, possibly 0.1 – 1
NGC 1068 (M 77)	43 100 240	0.02 – 0.18 0.036 0.022	0.16 – 129	0.2 0.2 0.2	0.36 0.02 0.02	129.0 129.0 129.0	0.35 0.016 0.015	$\lesssim 10^{-3}$

of the flux from the source at a given base frequency (third column). An important comment regarding flux values is as follows: there are currently no irrefutable arguments that the entire flux is related to the closest vicinity of the SMBH. This flux is actually smaller.

The fourth column displays a range of baseline projections for a given source that can be attained from the assumed orbit of the Millimetron telescope; the baseline projection range is normalized to Earth's diameter $D_{\rm Earth}$. Columns 5–8 show the minimum $D^{\rm min}/D_{\rm Earth}$ and maximum $D^{\rm max}/D_{\rm Earth}$ baseline projections and the expected correlated fluxes for which the source can be detected by the Millimetron observatory. The last column displays the ratio η of the source's X-ray and Eddington luminosity. The symbol 'n' shows that this value only refers to the nucleus.

4. Conclusions

We have considered the main types of accretion disks and jets for which radiation in the millimeter range due to synchrotron mechanism is of significance. As follows from this review, the main candidates for the role of accretion disks that radiate a significant part of their power in the millimeter (submillimeter) range are in the class of so-called radiatively inefficient flows, where the accretion rate of the black hole is much smaller than the characteristic Eddington value. Virtually all the SMBHs where scales of the order of the gravitational radius can be resolved in the current or planned VLBI experiments in the millimeter (submillimeter) band, such as the EHT or Millimetron, are in that class (Fig. 36). Observations with such a high resolution are only possible due to relatively short distances to those black holes, being of the order of several dozen Mpc. The only exceptions are objects with very massive black holes, among which the quasar OJ 287, a main candidate for a binary SMBH, is distinguished.

It is currently not clear whether the main source of millimeter radiation is a disk or a jet. This situation differs from that in the radio band, where jet radiation dominates. It is quite probable that relative power of the disk and jet vary from one source to another, an assumption that does not seem to disagree with our data on the spectral distribution of particular sources. We note, however, that this conclusion has been made within specific models of disks and jets.

The most important task for VLBI observations in the millimeter spectrum range is to directly observe the black hole image, its shadow. A favorable circumstance that may facilitate fulfilling this goal is that radiation-ineffective flows are probably optically thin in this part of the spectrum. This provides good grounds for the possible detection of the shadow. The shadow shape can be used to make qualitative conclusions about the main characteristics of black holes, such as their mass and angular momentum, the characteristics of the plasma that illuminates them, and the relative role of disks and jets in its formation. We note, however,

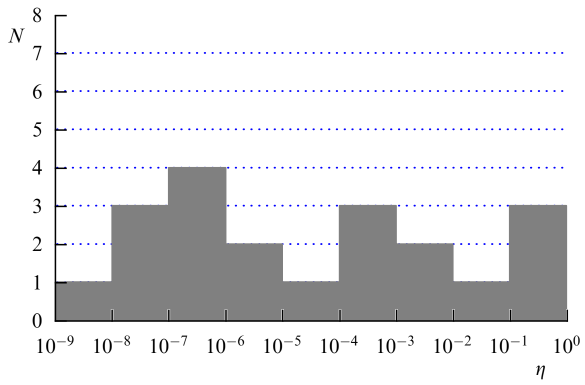

Figure 36. Histogram of the distribution of sources selected for observations using the Millimetron space observatory by the parameter η defined as a ratio of the bolometric and Eddington luminosities (we used the characteristic values of luminosity in a soft X-ray as an estimate for the sources for which the bolometric luminosity had not been found). The histogram is plotted for 20 selected objects; six of them are radiation sources strong enough ($\eta > 10^{-3}$) to suggest that the accretion flows within them are apparently not radiatively inefficient.

that significant difficulties are encountered in attempting to determine those characteristics. This is related to the large number of factors involved in shaping the shadow and the environment properties that could hinder observations (nonzero synchrotron self-absorption and scattering on plasma nonuniformities) and to the partial filling of the $u-v$ plane.

We have suggested a simple criterion for the detectability of objects with the Millimetron and the EHT. It assumes that the spatial distribution of a particular object's intensity is similar to that found in numerical simulation of the black hole in the galaxy M 87, while the absolute value is determined by the distance, the black hole mass, and the total radiation flow at the considered wavelength. This criterion has been applied to select about two dozen objects in a millimeter range to be observed by both the Millimetron and the EHT (Table 7). We emphasize that the quoted list is a preliminary one because it does not take specific features of particular objects into account. To develop a more reliable list, analytic and numerical simulations of specific sources of radiation using all other available data are needed. To reliably estimate the radiating area size, further observations of total fluxes in the

Table 7. Prospects for observation of SMBHs with the EHT.

Source	Frequency, GHz	Minimum base projection $/D_{\text{Earth}}$	Flux, Jy	Maximum base projection$/D_{\text{Earth}}$	Flux, Jy
Sgr A	84 211 240	0.0000046 0.0000046 0.0000046	2.400 4.100 4.100	0.8929736 0.8929736 0.8929736	0.429 0.148 0.146
NGC 4486 (M 87)	84 211 240	0.0000097 0.0000097 0.0000097	2.350 1.000 1.000	0.8560537 0.8560537 0.8560537	0.776 0.184 0.080
NGC 224	84 211 240	0.0000024 0.0000024 0.0000024	1.000 1.000 1.000	0.8560524 0.8560524 0.8560524	0.322 0.217 0.185
NGC 3842	84 211 240	0.0000080 0.0000080 0.0000080	0.300 0.800 0.800	0.8560520 0.8560520 0.8560520	0.210 0.283 0.294
NGC 4594	84 211 240	0.0000087 0.0000087 0.0000087	0.100 0.440 0.440	0.8938257 0.8938257 0.8938257	0.079 0.141 0.148
NGC 5128	84 211 240	0.0000009 0.0000009 0.0000009	41.000 6.000 6.000	0.8562899 0.8562899 0.8562899	40.608 5.645 5.544
NGC 1332	84 211 240	0.0000065 0.0000065 0.0000065	0.040 0.100 0.100	0.8938265 0.8938265 0.8938265	0.033 0.034 0.032
NGC 4374	84 211 240	0.0000096 0.0000096 0.0000096	0.140 0.100 0.100	0.8560516 0.8560516 0.8560516	0.127 0.053 0.044
NGC 4552	84 211 240	0.0000097 0.0000097 0.0000097	0.012 0.150 0.150	0.8560537 0.8560537 0.8560537	0.012 0.115 0.106
S5 0014 + 81	84 211 240	0.0000087 0.0000087 0.0000087	1.000 1.000 1.000	0.8560217 0.8560217 0.8560217	0.974 0.843 0.801
NGC 5077	84 211 240	0.0000085 0.0000085 0.0000085	0.660 0.400 0.400	0.8938265 0.8938265 0.8938265	0.651 0.367 0.358

Table 7. (continued)

Source	Frequency, GHz	Minimum base projection $/D_{\mathrm{Earth}}$	Flux, Jy	Maximum base projection $/D_{\mathrm{Earth}}$	Flux, Jy
Mrk 501	84 211 240	0.0000028 0.0000028 0.0000028	0.600 0.320 0.320	0.8560528 0.8560528 0.8560528	0.586 0.276 0.264
NGC 3031	84 211 240	0.0000058 0.0000058 0.0000058	0.400 0.180 0.180	0.8560538 0.8560538 0.8560538	0.394 0.164 0.159
OJ 287	84 211 240	0.0000080 0.0000080 0.0000080	4.500 3.000 3.000	0.8560530 0.8560530 0.8560530	4.451 2.797 2.740
Cygnus A	84 211 240	0.0000026 0.0000026 0.0000026	1.000 0.800 0.800	0.8560526 0.8560526 0.8560526	0.999 0.796 0.795
NGC 1316	84 211 240	0.0000025 0.0000025 0.0000025	1.400 2.500 2.500	0.8782765 0.8782765 0.8782765	1.396 2.458 2.446
NGC 6251	84 211 240	0.0000089 0.0000089 0.0000089	0.900 0.800 0.800	0.8557799 0.8557799 0.8557799	0.899 0.794 0.792
NGC 4258	84 211 240	0.0000011 0.0000011 0.0000011	0.010 0.020 0.020	0.8560531 0.8560531 0.8560531	0.010 0.020 0.020
NGC 1275	84 211 240	0.0000023 0.0000023 0.0000023	7.700 27.000 27.000	0.8560533 0.8560533 0.8560533	7.694 26.864 26.825
Her A (3C 348)	84 211 240	0.0000112 0.0000112 0.0000112	0.200 0.200 0.200	0.8560532 0.8560532 0.8560532	0.200 0.198 0.198

millimeter range are also required for both the objects included into our list and other interesting possible sources. The required observations can be performed using ALMA and, obviously, the EHT. An optimal strategy should be developed to determine the parameters of black holes and radiating plasma with consideration for insufficient filling of the $u-v$ plane, this aspect being of especial importance for the Millimetron project. We also note that the list of objects to be observed by the Millimetron apparently depends on the chosen spacecraft orbit.

A distinguishing specific feature of VLBI observations is that they can only find amplitudes and phases of some spatial harmonics of the source image that are determined by the available observational baselines and angular dimensions of the source. To fulfil the main tasks of VLBI observations in the millimeter band, it is important to develop accurate analytic and numerical models of specific sources, which can provide the missing information related to insufficient filling of the $u-v$ plane. An important related circumstance is that about half of the candidates for observations with the Millimetron and the EHT are, according to our criterion, the same objects. Joint observations of these objects by the EHT and Millimetron will enhance the $u-v$ plane filling and thus provide significantly broader information about spatial distributions of radiation intensity.

To conclude, we formulate some key tasks in this research area that, in our opinion, can be fulfilled by the planned Millimetron mission in the VLBI observation regime:

1. The Millimetron operating in the VLBI regime will be able to resolve the regions close to the event horizons of several dozen SMBHs located in the centers of the nearest galaxies, including ours. The Millimetron characteristics also enable resolving those areas for a number of rather distant bright objects (located at distances of the order of 10^3 Mpc), including the well-known sources 3C 273 and OJ 287. This will provide definitive evidence that black holes are the sources of activity in the centers of such galaxies and allow measuring the masses and angular momenta of these black holes.

2. Measuring radiation polarization and intensity on the horizon and lesser scales will enable determining whether the accretion disk or the jet makes the main contribution to their radiance, shedding light on jet formation mechanisms and the nature of turbulence in accretion disks.

Acknowledgments

This study was carried out with support from the Russian Foundation for Basic Research (grants 16-02-01043, 17-52-45053, 17-02-00788, and 19-02-00199) and was financed from the program of the Russian Academy of Sciences and the government contract for the Millimetron R&D. We are grateful to our colleagues at the Astro Space Center and Theoretical Department of the Lebedev Physical Institute, and especially to V S Beskin, I D Novikov, and S V Pilipenko for the numerous discussions and to I V Igumenshchev for a number of valuable comments.

Note added in proofs

When this review was under preparation for publication, the Event Horizon Telescope Collaboration published data obtained in spring 2017 on the intensity distribution of 1.3 mm wavelength radiation in the center of the galaxy M87 [99] and announced publishing data on radiation polarization. For the first time a quality image was obtained whose angular scale is comparable to the size of a black hole shadow, and the shadow has actually been observed. The image obtained contains a ring with an asymmetric brightness distribution having an angular diameter of about 40 ang. μs, which is somewhat smaller than that used by us (of the order of 60 ang. μs). The maximum brightness temperature of the ring is 6×10^9 K, and the total radiation flux ~ 0.5 Jy (see also [100]). The asymmetry of brightness distribution over the ring is interpreted as a manifestation of the Doppler boosting effect related to the ring rotation in the clockwise sense with respect to the observer located on Earth. The black hole mass thus obtained, $6.5 \times 10^9 M_\odot$, turned nut to be very close to that calculated using stellar dynamics methods. Characteristic estimates of physical parameters based on the assumption of the synchrotron character of radiation are close to the values that follow from Eqns (3) and (4). A more detailed simulation of the radiation formation used the models of radiation-inefficient accretion flows described above along with the assumption of thermal distribution of radiating electrons. Various rotation parameters and accretion disks were considered in both the MAD and 'normal evolution' regimes; the model was additionally constrained by a condition on the relativistic jet power that requires it to be larger than 10^{42} erg s^{-1} [100]. Unfortunately, rotation parameters of the black hole and some important characteristics of the accretion flow could not be reliably determined. This uncertainty is due to a rather low spatial resolution and insufficient filling of the $u-v$ plane. These issues may be unambiguously resolved in the framework of the Millimetron project.

References

1. Kardashev N S et al. *Phys. Usp.* **57** 1199 (2014); *Usp. Fiz. Nauk* **184** 1319 (2014)
2. Ho L C *Annu. Rev. Astron. Astrophys.* **46** 475 (2008)
3. Zhuravlev V V *Phys. Usp.* **58** 527 (2015); *Usp. Fiz. Nauk* **185** 561 (2015)
4. Paczynski B, Bisnovatyi-Kogan G S *Acta Astron.* **31** 283 (1981)
5. Abramowicz M A et al. *Astrophys. J.* **332** 646 (1988)
6. Yuan F, Quataert E, Narayan R *Astrophys. J.* **598** 301 (2003)
7. Narayan R, Yi I *Astrophys. J.* **428** L13 (1994)
8. Yuan F, Narayan R *Annu. Rev. Astron. Astrophys.* **52** 529 (2014)
9. Blandford R D, Begelman M C *Mon. Not. R. Astron. Soc.* **303** L1 (1999)
10. Yuan F, Bu D, Wu M *Astrophys. J.* **761** 130 (2012)
11. Narayan R, Igumenshchev I V, Abramowicz A A *Astrophys. J.* **539** 798 (2000)
12. Igumenshchev I V *Astrophys. J. Lett.* **577** L31 (2002)
13. Bisnovatyi-Kogan G S, Ruzmaikin A A *Astrophys. Space Sci.* **28** 45 (1974)
14. Bisnovatyi-Kogan G S, Ruzmaikin A A *Astrophys. Space Sci.* **42** 401 (1976)
15. Lubow S H, Papaloizou J C, Pringle J E *Mon. Not. R. Astron. Soc.* **267** 235 (1994)
16. Igumenschev I V *Astrophys. J.* **677** 317 (2008)
17. Shapiro S L, Lightman A P, Eardley D M *Astrophys. J.* **204** 187 (1976)
18. Nemmen R S, Storchi-Bergmann T, Eracleous M *Mon. Not. R. Astron. Soc.* **438** 2804 (2014)
19. Xie F-G, Yuan F *Mon. Not. R. Astron. Soc.* **427** 1580 (2012)
20. Ryan B R et al. *Astrophys. J. Lett.* **844** L24 (2017)
21. McKinney J C, Blandford R D *Mon. Not. R. Astron. Soc.* **394** L126 (2009)
22. Sokolovsky K V et al. *Astron. Astrophys.* **532** A38 (2011)
23. Blandford R D, Payne D G *Mon. Not. R. Astron. Soc.* **199** 883 (1982)
24. Blandford R D, Znajek R L *Mon. Not. R. Astron. Soc.* **179** 433 (1977)
25. Macdonald D, Thorne K S *Mon. Not. R. Astron. Soc.* **198** 345 (1982)
26. Armitage P J, Natarajan P *Astrophys. J.* **523** L7 (1999)
27. Bicknell G V, Begelman M C *Astrophys. J.* **467** 597 (1996)
28. Churazov E et al. *Mon. Not. R. Astron. Soc.* **332** 729 (2002)
29. Prieto M A et al. *Mon. Not. R. Astron. Soc.* **457** 3801 (2016)
30. Konigl A *Astrophys. J.* **243** 700 (1981)
31. Beskin V S *Phys. Usp.* **53** 1199 (2010); *Usp. Fiz. Nauk* **180** 1241 (2010)
32. Istomin Y N, Pariev V I *Mon. Not. R. Astron. Soc.* **281** 1 (1996)
33. Blandford R D, Konigl A *Astrophys. J.* **232** 34 (1979)
34. Piran T *Phys. Rep.* **314** 575 (1999)
35. Falcke H, Biermann P L *Astron. Astrophys.* **293** 665 (1995)
36. Hawley J *Astrophys. Space Sci.* **320** 107 (2009)
37. McKinney J C, Tchekhovskoy A, Blandford R D *Mon. Not. R. Astron. Soc.* **423** 3083 (2012)
38. Parfrey K, Giannios D, Beloborodov A M *Mon. Not. R. Astron. Soc.* **446** L61 (2016)
39. Ivanov P B, Illarionov A F *Mon. Not. R. Astron. Soc.* **285** 394 (1997)
40. Zhuravlev V V, Ivanov P B *Mon. Not. R. Astron. Soc.* **415** 2122 (2011)
41. Fragile P C, Anninos P *Astrophys. J.* **623** 347 (2005)
42. Zhuravlev V V et al. *Astrophys. J.* **796** 104 (2014)
43. Liska M et al. *Mon. Not. R. Astron.* **474** L81 (2017)
44. Yuan F et al. *Astrophys. J.* **598** 301 (2003)
45. Chandrasekhar S *The Mathematical Theory of Black Holes* (Oxford: Clarendon Press1983)
46. Frolov V P, Novikov I D *Black Hole Physics: Basic Concepts and New Developments* (Dordrecht: Kluwer, 1998)
47. Doeleman S S et al. *Nature* **455** 78 (2008)
48. Dexter J et al. *Astrophys. J.* **717** 1092 (2010)
49. Dexter J, McKinney J C, Agol E *Mon. Not. R. Astron. Soc.* **421** 1517 (2012)
50. Kuo C Y et al. *Astrophys. J.* **783** L33 (2014)
51. Marrone D P et al. *Astrophys. J.* **654** L57 (2007)
52. Moscibrodzka M et al. *Mon. Not. R. Astron. Soc.* **468** 2214 (2017)
53. Mao S A, Dexter J, Quataert E *Mon. Not. R. Astron. Soc.* **466** 4307 (2017)
54. Kamruddin A B, Dexter J *Mon. Not. R. Astron. Soc.* **434** 765 (2013)
55. Ricarte A, Dexter J *Mon. Not. R. Astron. Soc.* **446** 1973 (2015)
56. Gultekin K et al. *Astrophys. J.* **698** 198 (2009)
57. McConnell N J, PhD Theses (Berkeley, CA: Univ. of California, 2012)
58. Saglia R P et al. *Astrophys. J.* **818** 47 (2016)
59. Bosch R C E van den *Astrophys. J.* **831** 134 (2016)
60. Mikheeva E V et al. *Astron. Rep.* **63** 343 (2019); *Astron. Zh.* **96** 339 (2019)
61. Reid M *Int. J. Mod. Phys. D***18** 889 (2009)
62. Broderik A E et al. *Astrophys. J.* **735** 110 (2011)
63. Fish V L *Astrophys. J.* **727** L36 (2011)
64. Doeleman S et al. *Nature* **445** 78 (2008)
65. Moscibrodzka M et al., arXiv:1002.1261
66. Falcke H et al. *Astrophys. J.* **499** 731 (1998)
67. Marrone D P et al. *J. Phys. Conf. Ser.* **54** 354 (2006); *Proc. of "The Universe Under the Microscope — Astrophysics at High Angular Resolution", 21–25 April 2008, Bad Honnef, Germany* (Eds R Schoedel et al.) p. 354
68. An T et al. *Astrophys. J.* **634** L49 (2005)
69. Macquart J-P *Astrophys. J.* **646** L111 (2006)
70. Aitken D K et al. *Astrophys. J.* **534** L173 (2000)
71. Marrone D P *Astrophys. J.* **654** L57 (2006)
72. Marrone D P *Astrophys. J.* **640** 308 (2006)
73. Walker R C et al. *J. Phys. Conf. Ser.* **131** 012053 (2008)
74. Walsh J L et al. *Astrophys. J.* **770** 86 (2013)
75. Gebhardt K et al. *Astrophys. J.* **729** 119 (2011)
76. Junor W, Biretta J A, Livio M *Astrophys. J.* **401** 891 (1999)
77. Ly C, Walker R C, Wrobel J M *Astron. J.* **127** 119 (2004)

78. Kovalev Y Y et al. *Astrophys. J.* **668** L27 (2007)
79. Biretta J A, Sparks W B, Macchetto F *Astrophys. J.* **520** 621 (1999)
80. Cheung C C, Harris D E, Stawarz L *Astrophys. J.* **663** L65 (2007)
81. Owen F N, Eilek J A, Keel W C *Astrophys. J.* **362** 449 (1990)
82. Algaba J C, Asada, K, Nakamura M *Astrophys. J.* **823** 86 (2016)
83. Zavala R T, Taylor G B *Astrophys. J.* **566** L9 (2002)
84. Kuo C Y et al. *Astrophys. J.* **783** L33 (2014)
85. Peterson B M *Space Sci. Rev.* **183** 253 (2014)
86. Hernandez-Toledo H M, Ortega-Esbri S *Astron. Astrophys.* **487** 485 (2008)
87. Kuntschner H *Mon. Not. R. Astron. Soc.* **369** 497 (2006)
88. Tornikoski M et al. *Astron. J.* **121** 1306 (2011)
89. Wilman R J, Edge A C, Johnstone R M *Mon. Not. R. Astron. Soc.* **359** 755 (2005)
90. Nelson C H et al. *Astrophys. J.* **544** L91 (2000)
91. Bentz M C, Katz S *Publ. Astron. Soc. Pacific* **127** 67 (2015)
92. Bruni G et al. *Astron. Astrophys.* **604** A111 (2017)
93. Gandhi P et al. *Astron. Astrophys.* **502** 457 (2009)
94. Valtonen M J, Ciprini S, Lehto H J *Mon. Not. R. Astron. Soc.* **427** 77 (2012)
95. Daly R A *Astrophys. J.* **691** 72 (2009)
96. Gaffney N I, Lester D F, Telesco C M *Astrophys. J.* **407** L57 (1993)
97. Ghisellini G et al. *Mon. Not. R. Astron. Soc.* **405** 387 (2010)
98. Woo J H et al. *Astrophys. J.* **631** 762 (2005)
99. Akiyama K et al. (Event Horizon Telescope Collab.) *Astrophys. J. Lett.* **875** L1 (2019)
100. Akiyama K et al. (Event Horizon Telescope Collab.) *Astrophys. J. Lett.* **875** L5 (2019)